

Role of various scale-similarity models in stabilized mixed subgrid-scale model

Kazuhiro Inagaki^{1, a)} and Hiromichi Kobayashi²

¹⁾*Institute of Industrial Science, The University of Tokyo, 4-6-1 Komaba, Meguro-ku, Tokyo 153-8505, Japan*

²⁾*Department of Physics & Research and Education Center for Natural Sciences, Hiyoshi Campus, Keio University, 4-1-1 Hiyoshi, Kohoku-ku, Yokohama 223-8521, Japan*

(Dated: 24 December 2021)

We investigate the physical role of various scale-similarity models in the stabilized mixed model [K. Abe, *Int. J. Heat Fluid Flow*, **39**, 42 (2013); M. Inagaki and K. Abe, *Int. J. Heat Fluid Flow*, **64**, 137 (2017)] and evaluate their performance in turbulent channel flows. Among various models in the present study, the original model combined with the scale-similarity model for the subgrid-scale (SGS)-Reynolds term yields the best prediction for the anisotropy of the grid-scale (GS) velocity fluctuations and the SGS stress, even in coarse grid resolutions. Moreover, it successfully predicts large intensities of the spectra close to the cut-off scale in accordance with the filtered direct numerical simulation, whereas other models predict a rapid decay of the spectra in the low-wavelength region. To investigate the behavior of the models close to the cut-off scale, we analyze the budget equation for the GS Reynolds stress spectrum. The result shows that the scale-similarity model for the SGS-Reynolds term plays a role in the enhancement of the wall-normal velocity fluctuation close to the cut-off scale. Thereby, it activates turbulence close to the cut-off scale, leading to a reproduction of the proper streak structures observed in wall-bounded turbulent flows. The reproduction of velocity fluctuations close to the cut-off scale and turbulent structures is a key element for further development of SGS models.

^{a)}Electronic mail: kinagaki@iis.u-tokyo.ac.jp

I. INTRODUCTION

Large-eddy simulation (LES) is an essential tool employed to predict high-Reynolds-number turbulent flows. LES solves large-scale or grid-scale (GS, resolved scale, or super-filter scale) eddies in turbulent flows. Meanwhile, effects of subgrid-scale (SGS, unresolved, or sub-filter scale) turbulent eddies are modeled. This procedure is referred to as SGS modeling. SGS modeling was studied for half a century since the pioneering work by Smagorinsky¹. Numerous practical SGS models, including the Smagorinsky model¹, are based on the linear eddy-viscosity assumption, which models the effect of SGS eddies as an effective viscosity. To date, several eddy-viscosity type models have been proposed, e.g., dynamic models²⁻⁴, one-equation models^{2,5,6}, and modified local eddy-viscosity models⁷⁻⁹. Recently, LES approach is also applied to the lattice-Boltzmann method, employing the eddy-viscosity concept¹⁰.

Although the eddy-viscosity models are simple and handy, their physical reliability are not sufficient. Several studies showed that the principal axis of the exact SGS stress tensor does not generally align with that of the strain rate tensor¹¹⁻¹⁵. Hence, the eddy-viscosity models cannot reproduce the exact property of the SGS stress tensor; however, they are reasonable for estimation of the energy transfer rate from the GS to SGS fields^{9,11}. A traditional approach to improve the SGS model is to employ scale-similarity models¹². Scale-similarity models were shown to yield a better correlation with the exact SGS stress than eddy-viscosity models¹¹⁻¹⁶. However, such scale-similarity models are not sufficiently dissipative to be employed by themselves for a stable performance of the LES. Moreover, scale-similarity models cause backscatter or energy transfer from the SGS to GS fields^{13,14,17,18}, which can induce numerical instability. A remedy for these difficulties is to combine scale-similarity models with the eddy-viscosity model. The resulting model is referred to as the mixed model, which was first proposed by Bardina *et al.*¹². Several types of mixed models have been suggested to date (see, Refs. 13, 19-26). However, the backscatter caused by scale-similarity models still makes the mixed model difficult to apply it to engineering problems with complex geometries. Furthermore, Anderson and Domaradzki²⁷ showed that the conventional scale-similarity model yields an excessive dissipation directly from the largest resolved scales, which is unphysical in the sense of localness in scale of energy transfer. In this sense, the physics of scale-similarity models itself also needs to be discussed in detail. As another branch of recent developments of SGS modeling, algebraic stress modeling approach, which was first developed in the Reynolds-averaged Navier–Stokes (RANS) modeling (see, e.g.,

Refs. 28–31), was discussed and its performance was evaluated^{32–34}.

For practical use of the SGS model, both applicability and physical consistency of the model are required. As a unique approach to utilize the physics of scale-similarity models in a numerically stable manner, Abe³⁵ proposed a new formalism of the mixed model, which is referred to as the stabilized mixed model (SMM). Further discussion on the modification or other modeling approaches of the SMM are provided in Refs. 16, 36, and 37. Surprisingly, the SMM is significantly less sensitive to the grid resolution than conventional eddy-viscosity models^{35,38,39}. Moreover, overestimation of the streamwise velocity fluctuation, which is often observed in the LES at coarse grid resolutions, decreases significantly, yielding a better prediction of the anisotropy of the GS velocity fluctuations in comparison with the direct numerical simulation (DNS). However, the physical mechanism that the SMM yields better results is still under discussion. Otsuka and Abe³⁸ showed that the SMM maintains streamwise vortices even at coarse grid resolutions in turbulent channel flows, hence reproducing the mean velocity profile. Abe⁴⁰ showed that the non-eddy-viscosity term contributes significantly to the generation of the GS Reynolds shear stress in the channel flow by performing an *a priori* test. These results suggest that a non-eddy-viscosity term is a key element to improve physical properties of SGS models.

In the SMM, Abe³⁵ adopted the scale-similarity model for the SGS-Reynolds term, following the suggestion of Horiuti⁴¹, on the proper velocity scale for the SGS energy. However, previous studies show that other scale-similarity models yield better correlations with the exact SGS stress^{11–16}. In this sense, physical consistency and reliability of the SMM are still unclear, albeit its attractive performance. If the SMM is used without understanding the physical properties, the results of the SMM could not be evaluated exactly in its application to turbulent flows. Therefore, it is required to reveal physical properties of the SMM. To understand the physics of the SMM is helpful for further development of SGS modeling. Now, we pose a question regarding which scale-similarity model exhibits the best performance in predicting turbulent flows. To investigate the physics of SGS models, we should analyze their properties in their applications to numerical simulations; namely, *a posteriori* tests. In the present study, we construct the SMM using various scale-similarity models and evaluate their performance in turbulent channel flows.

The rest of this paper is organized as follows. In Sec. II, we describe the modeling procedure of the SMM³⁵. In Sec. III, we construct various types of SMMs and evaluate their performance in turbulent channel flows. In this section, we find that the reproduction of the GS and SGS anisotropies significantly depends on SGS models, through the Lumley’s invariant map. Moreover,

we address that the critical difference among the models lies in the low-wavelength region of the GS Reynolds spectrum. To investigate the physical origin of the difference in the low-wavelength region, we discuss the budget for the GS Reynolds stress spectrum^{43–45} in Sec. IV. In this section, we also discuss the relation between the spectrum and the streak structures observed in wall-bounded turbulent flows. Conclusions are given in Sec V.

II. STABILIZED MIXED MODEL WITH VARIOUS SCALE-SIMILARITY TERMS

A. Governing equations and scale-similarity models

The governing equations in LES for an incompressible fluid are the filtered continuity and Navier–Stokes equations:

$$\frac{\partial \bar{u}_i}{\partial x_i} = 0, \quad (1)$$

$$\frac{\partial \bar{u}_i}{\partial t} = -\frac{\partial}{\partial x_j} (\bar{u}_i \bar{u}_j + \tau_{ij}^{\text{sgs}}) - \frac{\partial \bar{p}}{\partial x_i} + \frac{\partial}{\partial x_j} (2\nu \bar{s}_{ij}), \quad (2)$$

where $\bar{\cdot}$ denotes the filtering operation, \bar{u}_i is the GS velocity, $\tau_{ij}^{\text{sgs}} (= \overline{u_i u_j} - \bar{u}_i \bar{u}_j)$ is the SGS stress, \bar{p} is the pressure divided by the density, ν is the kinematic viscosity, and $\bar{s}_{ij} [= (\partial \bar{u}_i / \partial x_j + \partial \bar{u}_j / \partial x_i) / 2]$ is the GS strain rate. To close the equations, we must model the SGS stress τ_{ij}^{sgs} . A conventional model for τ_{ij}^{sgs} is an eddy-viscosity type model:

$$\tau_{ij}^{\text{sgs}} = \frac{1}{3} \tau_{\ell\ell}^{\text{sgs}} \delta_{ij} - 2\nu^{\text{sgs}} \bar{s}_{ij}, \quad (3)$$

where ν^{sgs} denotes the SGS eddy viscosity. A widely accepted expression for ν^{sgs} was proposed by Smagorinsky¹, which expresses ν^{sgs} through the filter width $\bar{\Delta}$ and the GS strain rate $\bar{s}_{ij} \bar{s}_{ij}$. The dynamic approach^{2–4} extends applicability of the Smagorinsky model¹ to more complex turbulent flows. However, these models involve an intrinsic shortfall of negative viscosity, which causes exponential divergence^{2,23}. As a remedy, other local expressions for ν^{sgs} have been proposed^{7–9}.

Although the eddy-viscosity models are simple and handy, several studies showed that the strain rate tensor does not necessarily align with the exact SGS stress^{11–15}. An approach to improve this problem is to employ scale-similarity models¹². Conventionally, the SGS stress is decomposed

into the following three terms⁴⁶:

$$\tau_{ij}^{\text{sgs}} = \mathcal{L}_{ij} + \mathcal{C}_{ij} + \mathcal{R}_{ij}, \quad (4a)$$

$$\mathcal{L}_{ij} = \overline{\bar{u}_i \bar{u}_j} - \bar{u}_i \bar{u}_j, \quad (4b)$$

$$\mathcal{C}_{ij} = \overline{\bar{u}_i u_j'} + \overline{u_i' \bar{u}_j}, \quad (4c)$$

$$\mathcal{R}_{ij} = \overline{u_i' u_j'}, \quad (4d)$$

where $u_i' = u_i - \bar{u}_i$. We refer to \mathcal{L}_{ij} , \mathcal{C}_{ij} , and \mathcal{R}_{ij} as the Leonard, cross, and SGS-Reynolds terms, respectively. Note that the sum of the Leonard and cross terms satisfy the Galilean invariance, although the individual terms do not⁴⁷. The scale-similarity assumption¹² gives the approximation $\overline{u_i' u_j} \simeq \overline{u_i'} \bar{u}_j$. Under this scale-similarity assumption, the cross and SGS-Reynolds terms, Eqs. (4c) and (4d), yield

$$\mathcal{C}_{ij} \simeq \overline{\bar{u}_i u_j'} + \overline{u_i' \bar{u}_j} = \bar{u}_i (\bar{u}_j - \bar{u}_j) + (\bar{u}_i - \bar{u}_i) \bar{u}_j, \quad (5a)$$

$$\mathcal{R}_{ij} \simeq \overline{u_i' u_j'} = (\bar{u}_i - \bar{u}_i) (\bar{u}_j - \bar{u}_j). \quad (5b)$$

The sum of \mathcal{L}_{ij} , \mathcal{C}_{ij} , and \mathcal{R}_{ij} under the scale-similarity assumption reads

$$\mathcal{L}_{ij} + \mathcal{C}_{ij} + \mathcal{R}_{ij} \simeq \mathcal{L}_{ij}^{\text{m}} = \overline{\bar{u}_i \bar{u}_j} - \bar{u}_i \bar{u}_j, \quad (6)$$

where $\mathcal{L}_{ij}^{\text{m}}$ is referred to as the modified Leonard term, which is a redefined Leonard term employed to satisfy the Galilean invariance⁴⁸. Employing the Gaussian or top-hat filter as the test filter, the Taylor expansion of the filtered velocity yields

$$\widehat{\bar{u}}_i = \bar{u}_i + \frac{\widehat{\Delta}_\ell^2}{24} \frac{\partial^2 \bar{u}_i}{\partial x_\ell \partial x_\ell} + O(\widehat{\Delta}^4), \quad (7)$$

where the test filter operation $\widehat{\cdot}$ is used to explicitly show which filter is expanded, and $\widehat{\Delta}_i$ is the filter width in the x_i direction accompanied with $\widehat{\cdot}$. Hence, the modified Leonard term is expanded as

$$\begin{aligned} \mathcal{L}_{ij}^{\text{m}} &= C_{ij} - \frac{\overline{\Delta}_\ell^2}{24} \frac{\partial^2 \bar{u}_i}{\partial x_\ell \partial x_\ell} \frac{\overline{\Delta}_m^2}{24} \frac{\partial^2 \bar{u}_j}{\partial x_m \partial x_m} + O(\overline{\Delta}^4) \\ &= C_{ij} + O(\overline{\Delta}^4), \end{aligned} \quad (8)$$

$$C_{ij} = \frac{\overline{\Delta}_\ell^2}{12} \frac{\partial \bar{u}_i}{\partial x_\ell} \frac{\partial \bar{u}_j}{\partial x_\ell}, \quad (9)$$

where C_{ij} is referred to as the Clark term. The second term on the first line of Eq. (8) corresponds to the Taylor expansion of the scale-similarity model for the SGS-Reynolds term \mathcal{R}_{ij} ;

$$\mathcal{R}_{ij} \simeq \frac{\bar{\Delta}_\ell^2}{24} \frac{\partial^2 \bar{u}_i}{\partial x_\ell \partial x_\ell} \frac{\bar{\Delta}_m^2}{24} \frac{\partial^2 \bar{u}_j}{\partial x_m \partial x_m}. \quad (10)$$

In this paper, we refer to terms expressed by Eqs. (5a), (5b), (6), and (9) as scale-similarity models.

B. Stabilized mixed model

Abe³⁵ proposed the following mixed model, referred to as the SMM:

$$\begin{aligned} \tau_{ij}^{\text{sgs}} &= \frac{2}{3} k^{\text{sgs}} \delta_{ij} - 2\nu^{\text{sgs}} \bar{s}_{ij} + \tau_{ij}^{\text{eat}}, \\ \tau_{ij}^{\text{eat}} &= 2k^{\text{sgs}} \frac{\tau_{ij}^{\text{a}}|_{\text{tl}} + 2\nu^{\text{a}} \bar{s}_{ij}}{\tau_{\ell\ell}^{\text{a}}}, \quad \nu^{\text{a}} = -\frac{\tau_{ij}^{\text{a}}|_{\text{tl}} \bar{s}_{ij}}{2\bar{s}_{\ell m} \bar{s}_{\ell m}}, \\ \nu^{\text{sgs}} &= C_{\text{sgs}} f_v \bar{\Delta} \sqrt{k^{\text{sgs}}}, \end{aligned} \quad (11)$$

Here, $k^{\text{sgs}} (= \tau_{\ell\ell}^{\text{sgs}}/2)$ is the SGS kinetic energy, ν^{sgs} is the SGS eddy viscosity, $A_{ij}|_{\text{tl}} = A_{ij} - A_{\ell\ell} \delta_{ij}/3$, τ_{ij}^{a} denotes an additional term, and C_{sgs} is a constant. f_v is the wall damping function based on the Kolmogorov scale^{36,49}:

$$\begin{aligned} f_v &= 1 - \exp[-(d_\varepsilon/A_0)^{2/(1+C_0)}], \\ d_\varepsilon &= \frac{u_\varepsilon n}{\nu} \left(\frac{n}{\bar{\Delta}}\right)^{C_0}, \quad u_\varepsilon = (\nu \varepsilon^{\text{sgs}})^{1/4}, \\ \varepsilon^{\text{sgs}} &= C_\varepsilon \frac{(k^{\text{sgs}})^{3/2}}{\bar{\Delta}} + \varepsilon^{\text{wall}}, \quad \varepsilon^{\text{wall}} = \frac{2\nu k^{\text{sgs}}}{n^2}, \end{aligned} \quad (12)$$

where n denotes the distance from the nearest solid wall, ε^{sgs} denotes the SGS energy dissipation rate, and C_ε , A_0 , and C_0 are constants. We refer to τ_{ij}^{eat} in Eq. (11) as the extra anisotropic term (EAT). In the original model³⁵, an unusual filter scale, $\bar{\Delta} = \sqrt{\max(\Delta x \Delta y, \Delta y \Delta z, \Delta z \Delta x)}$ in Cartesian coordinates, is adopted. Inagaki and Abe³⁶ modified this unusual filter scale to the conventional one, $\bar{\Delta} = (\Delta x \Delta y \Delta z)^{1/3}$ in Cartesian coordinates, and set the model constants in $C_{\text{sgs}} = 0.075$, $C_\varepsilon = 0.835$, $A_0 = 13$, and $C_0 = 1/3$. The SGS kinetic energy k^{sgs} is obtained by numerically solving the following model equation:

$$\begin{aligned} \frac{\partial k^{\text{sgs}}}{\partial t} &= -\frac{\partial}{\partial x_j} (\bar{u}_j k^{\text{sgs}}) - \tau_{ij}^{\text{sgs}} \bar{s}_{ij} - \varepsilon^{\text{sgs}} \\ &\quad + \frac{\partial}{\partial x_j} \left[\left(\nu + C_k f_v \bar{\Delta} \sqrt{k^{\text{sgs}}} \right) \frac{\partial k^{\text{sgs}}}{\partial x_j} \right], \end{aligned} \quad (13)$$

where f_v and ε^{sgs} are defined in Eq. (12) and C_k is set as $C_k = 0.1$.

There are two notable features on the SMM. First, the v^a related term is introduced to remove the backscatter and stabilize the model; namely, we have

$$\bar{s}_{ij}\tau_{ij}^{\text{eat}} = 2k^{\text{sgs}} \frac{\bar{s}_{ij}\tau_{ij}^a|_{\text{td}} + 2v^a\bar{s}_{ij}\bar{s}_{ij}}{\tau_{\ell\ell}^a} = 0, \quad (14)$$

which indicates that the last term on the first line of Eq. (11) does not contribute to the energy transfer between the GS and SGS fields. Thereby, the second term on the right-hand side of Eq. (13) yields

$$-\tau_{ij}^{\text{sgs}}\bar{s}_{ij} = 2v^{\text{sgs}}\bar{s}_{ij}\bar{s}_{ij} \geq 0, \quad (15)$$

which indicates the absence of backscatter because $v^{\text{sgs}} \geq 0$. Hence, we calculate Eq. (13) in a numerically stable manner when utilizing scale-similarity models. Because Eq. (13) does not necessarily guarantee the positiveness of k^{sgs} , we must clip the negative value of k^{sgs} in the numerical simulation. Otherwise, v^{sgs} , which is proportional to $\sqrt{k^{\text{sgs}}}$, cannot be calculated.

Second, the EAT is expressed by a form of the normalized anisotropy tensor:

$$\tau_{ij}^{\text{eat}} = 2k^{\text{sgs}} \left(\frac{\tau_{ij}^a + 2v^a\bar{s}_{ij}}{\tau_{\ell\ell}^a + 2v^a\bar{s}_{\ell\ell}} - \frac{1}{3}\delta_{ij} \right) = 2k^{\text{sgs}}b_{ij}^a. \quad (16)$$

The advantage of this normalized form is that the model can predict the anisotropy of the SGS field even when a component of τ_{ij}^a becomes small. This is because the denominator $\tau_{\ell\ell}^a$ decreases at the same rate as τ_{ij}^a . Owing to these two features, we can make full use of scale-similarity models in a numerically stable manner.

In this study, we note that Abe³⁵ or Inagaki and Abe³⁶ adopted

$$\tau_{ij}^a = (\bar{u}_i - \widehat{u}_i)(\bar{u}_j - \widehat{u}_j), \quad (17)$$

for the EAT. Equation (17) corresponds to the scale-similarity model for the SGS-Reynolds term (5b), although the repeated filter operation of $\bar{\cdot}$ is replaced with the test filter operation $\widehat{\cdot}$. Because the stabilization procedure of Abe³⁵ is independent of the choice of τ_{ij}^a , we can construct various types of SMMs, by for example using the modified Leonard term \mathcal{L}_{ij}^m (6) or the Clark term C_{ij} (9). Considering the results of numerous previous studies addressing the correlation between scale-similarity models and the exact SGS stress¹¹⁻¹⁶, we expect that the modified Leonard or Clark terms yield a better performance in the reproduction of the physics of turbulent flows in the LES than the scale-similarity model for the SGS-Reynolds term. In the following section, we construct the SMM using various scale-similarity models and evaluate their performance in turbulent channel flows as a typical case of wall-bounded turbulent shear flows.

III. STATISTICS OF VARIOUS STABILIZED MIXED MODELS IN TURBULENT CHANNEL FLOWS

A. Variety of stabilized mixed models

We construct various SMMs based on the model suggested by Inagaki and Abe³⁶(hereafter denoted as IA), which was modified from the original model³⁵ to enable the use of the conventional filter scale $\bar{\Delta} = (\Delta x \Delta y \Delta z)^{1/3}$ in Cartesian coordinates. In the construction, we fix all model constants described in Sec. II B except C_{sgs} for the cases excluding the EAT and only change τ_{ij}^a , which is the scale-similarity model for the SGS-Reynolds term (17) in the original model. The applied models are listed in the followings:

1. Original IA model³⁶ (IA):

$$\tau_{ij}^a = (\bar{u}_i - \hat{u}_i)(\bar{u}_j - \hat{u}_j),$$

2. IA model with the Clark term (IA-CL):

$$\tau_{ij}^a = \frac{\bar{\Delta}_\ell^2}{12} \frac{\partial \bar{u}_i}{\partial x_\ell} \frac{\partial \bar{u}_j}{\partial x_\ell}$$

3. IA model with the modified Leonard term (IA-ML):

$$\tau_{ij}^a = \bar{u}_i \bar{u}_j - \bar{\bar{u}}_i \bar{\bar{u}}_j$$

4. IA model with the stress based on the Laplacian of velocity (IA-LV):

$$\tau_{ij}^a = \bar{\Delta}^4 (\nabla^2 \bar{u}_i) (\nabla^2 \bar{u}_j)$$

5. IA model without the EAT (IA-LN):

$$\tau_{ij}^a = 0$$

In addition to the conventional scale-similarity models, we test a model based on the Laplacian of velocity (IA-LV). The scale-similarity model for the SGS-Reynolds term is reduced to this LV model through the Taylor expansion using a cubic grid:

$$\begin{aligned} (\bar{u}_i - \hat{u}_i)(\bar{u}_j - \hat{u}_j) &= \frac{\hat{\Delta}_\ell^2}{24} \frac{\partial^2 \bar{u}_i}{\partial x_\ell \partial x_\ell} \frac{\hat{\Delta}_m^2}{24} \frac{\partial^2 \bar{u}_j}{\partial x_m \partial x_m} \\ &= \frac{\gamma^4}{24^2} \bar{\Delta}^4 (\nabla^2 \bar{u}_i) (\nabla^2 \bar{u}_j), \end{aligned} \quad (18)$$

where $\gamma = \widehat{\Delta}_\alpha / \overline{\Delta}_\alpha (= \text{const.})$. Note that the SMM does not depend on the value of the coefficient $\gamma^4 / 24^4$ because τ_{ij}^a is normalized, as shown in Eqs. (11) or (16). For the numerical simulation of turbulent channel flows, we often employ a rectangular grid, such that IA and IA-LV yield different results.

B. Computational methods and numerical conditions

We employ a Cartesian coordinate grid and set the streamwise, wall-normal, and spanwise directions as $x(=x_1)$, $y(=x_2)$, and $z(=x_3)$, respectively. We use the staggered grid system and adopt the fully conservative central finite difference scheme⁵⁰ for the x and z directions with fourth-order accuracy and the conservative central finite difference scheme on non-uniform grids⁵¹ for the y direction with second-order accuracy, for both equations for the velocity and SGS kinetic energy k^{sgs} . The boundary condition is periodic in the x and z directions and it is no slip in the y direction. The Poisson equation for pressure is solved using a fast Fourier transformation. For time marching in the velocity field, we adopt the second-order Adams–Bashforth method. For time marching in k^{sgs} , we adopt the explicit Euler method, except for the dissipation term ε^{sgs} , which is treated implicitly. For the test filtering operation, we approximate it through the Taylor expansion as Eq. (7). The spatial derivative for each direction in Eq. (7) is discretized with second-order accuracy, i.e., we discretize $\widehat{q}^{(I,J,K)}$ as

$$\begin{aligned} \widehat{q}^{(I,J,K)} = & \overline{q}^{(I,J,K)} + \frac{\widehat{\Delta}_x^2}{24} \frac{\overline{q}^{(I-1,J,K)} - 2\overline{q}^{(I,J,K)} + \overline{q}^{(I+1,J,K)}}{\Delta x^2} \\ & + \frac{\widehat{\Delta}_y^2}{24} \frac{1}{\Delta y^{(J)}} \left[-\frac{\overline{q}^{(I,J-1,K)} + \overline{q}^{(I,J,K)}}{\Delta y^{(J-1/2)}} \right. \\ & \quad \left. + \frac{\overline{q}^{(I,J,K)} + \overline{q}^{(I,J+1,K)}}{\Delta y^{(J+1/2)}} \right] \\ & + \frac{\widehat{\Delta}_z^2}{24} \frac{\overline{q}^{(I,J,K-1)} - 2\overline{q}^{(I,J,K)} + \overline{q}^{(I,J,K+1)}}{\Delta z^2} \\ & + O(\Delta x^4) + O(\Delta y^4) + O(\Delta z^4), \end{aligned} \quad (19)$$

where the superscript (I, J, K) denotes the grid point. Because $\widehat{\Delta}_i \propto \Delta x_i$, the test-filtered variables retain fourth-order accuracy in the central finite difference scheme. We set $\overline{\Delta}_i = \Delta x_i$, $\widehat{\Delta}_i = 2\overline{\Delta}_i$, and $\widehat{\Delta}_i = \sqrt{3} \overline{\Delta}_i$ to satisfy $\overline{\Delta}_\alpha^2 + \widehat{\Delta}_\alpha^2 = \widehat{\Delta}_\alpha^2$, which is satisfied when the Gaussian filter is employed as the test filter⁴⁶. We perform two Reynolds number cases, $\text{Re}_\tau = 180$ and $\text{Re}_\tau = 1000$ where

$\text{Re}_\tau (= u_\tau h / \nu)$ is the Reynolds number based on the channel half width h and the wall friction velocity $u_\tau (= \sqrt{|\partial U_x / \partial |_{\text{wall}}|})$, where $U_x (= \langle \bar{u}_x \rangle)$ is the streamwise mean velocity and $\langle \cdot \rangle$ denotes the statistical average. In the present simulation, we adopt the average over the x - z plane and time to obtain the statistical average. For $\text{Re}_\tau = 180$, we perform a DNS with the same discretization method as the present LES.

Flow cases and numerical parameters are listed in Table I. For $\text{Re}_\tau = 180$, we evaluate the grid resolution dependency of the representative models and set three grid resolution cases; low resolution (LR), where $\Delta x^+ = 94$ and $\Delta z^+ = 47$; medium resolution (MR), where $\Delta x^+ = 47$ and $\Delta z^+ = 24$; high resolution (HR), where $\Delta x^+ = 94$ and $\Delta z^+ = 47$, while Δy^+ is fixed. Values with a superscript ‘+’ denote those normalized by u_τ and ν . Further, we perform the simulations with the same resolution as LR, but in a large domain (LD), where $L_x = 16\pi h$ and $L_z = 16\pi h/3$ to obtain smooth profile spectra. For IA-LN in LR at $\text{Re}_\tau = 180$, the value $C_{\text{sgs}} = 0.075$, which is optimized for IA³⁶ is too large to sustain the GS turbulent fluctuation. Hence, we establish a reference linear eddy-viscosity model case with a smaller coefficient $C_{\text{sgs}} = 0.042$ (IA-LNcs42), which is optimized for an one-equation eddy-viscosity model⁴⁹. To evaluate the filtered values in the *a priori* test through the DNS result, we adopt the sharp cut-off filter in the Fourier space in the x and z directions, while no filtering operation is applied in the y direction. The filter scale is set in $\bar{\Delta}_x^+ = 94$ and $\bar{\Delta}_z^+ = 47$ to the same value as the LR cases in LES.

To investigate a higher Reynolds number case, we perform LES at $\text{Re}_\tau = 1000$. At this Reynolds number, we perform a low resolution (LR) simulation, where $\Delta x^+ = 65$ and $\Delta z^+ = 49$, in which the spanwise resolution is almost the same as in LR at $\text{Re}_\tau = 180$. For IA, we additionally perform a very low resolution (VLR) case, where $\Delta x^+ = 130$ and $\Delta z^+ = 98$.

C. Basic statistics

1. Mean velocity for basic models

Figure 1 shows the mean velocity profile for (a) DSM, (b) IA-LN, and (c) IA at various grid resolutions or domain sizes at $\text{Re}_\tau = 180$. We plot the no-model result in Fig. 1(d) for reference. In LR, all cases except for IA overestimate the mean velocity. The IA model provides a good prediction irrespective of the grid resolution. In Fig. 1(c), IA-LN180LR excessively overestimates the mean velocity. This is because the GS velocity fluctuations disappear. However, this does not

TABLE I. Flow cases and numerical parameters.

Case	Re_τ	$L_x \times L_y \times L_z$	$N_x \times N_y \times N_z$	Δx^+	Δy^+	Δz^+	C_{sgs}
IA180LR	180	$4\pi h \times 2h \times 4\pi h/3$	$24 \times 64 \times 16$	94	1.1–11	47	0.075
IA180MR	180	$4\pi h \times 2h \times 4\pi h/3$	$48 \times 64 \times 32$	47	1.1–11	24	0.075
IA180HR	180	$4\pi h \times 2h \times 4\pi h/3$	$96 \times 64 \times 64$	24	1.1–11	12	0.075
IA180LD	180	$16\pi h \times 2h \times 16\pi h/3$	$96 \times 64 \times 64$	94	1.1–11	47	0.075
IA-CL180LR	180	$4\pi h \times 2h \times 4\pi h/3$	$24 \times 64 \times 16$	94	1.1–11	47	0.075
IA-CL180LD	180	$16\pi h \times 2h \times 16\pi h/3$	$96 \times 64 \times 64$	94	1.1–11	47	0.075
IA-ML180LR	180	$4\pi h \times 2h \times 4\pi h/3$	$24 \times 64 \times 16$	94	1.1–11	47	0.075
IA-LV180LR	180	$4\pi h \times 2h \times 4\pi h/3$	$24 \times 64 \times 16$	94	1.1–11	47	0.075
IA-LN180LR	180	$4\pi h \times 2h \times 4\pi h/3$	$24 \times 64 \times 16$	94	1.1–11	47	0.075
IA-LNcs42-180LR	180	$4\pi h \times 2h \times 4\pi h/3$	$24 \times 64 \times 16$	94	1.1–11	47	0.042
IA-LNcs42-180MR	180	$4\pi h \times 2h \times 4\pi h/3$	$48 \times 64 \times 32$	47	1.1–11	24	0.042
IA-LNcs42-180HR	180	$4\pi h \times 2h \times 4\pi h/3$	$96 \times 64 \times 64$	24	1.1–11	12	0.042
IA-LNcs42-180LD	180	$16\pi h \times 2h \times 16\pi h/3$	$96 \times 64 \times 64$	94	1.1–11	47	0.042
DSM180LR	180	$4\pi h \times 2h \times 4\pi h/3$	$24 \times 64 \times 16$	94	1.1–11	47	-
DSM180MR	180	$4\pi h \times 2h \times 4\pi h/3$	$48 \times 64 \times 32$	47	1.1–11	24	-
DSM180HR	180	$4\pi h \times 2h \times 4\pi h/3$	$96 \times 64 \times 64$	24	1.1–11	12	-
no-model180LR	180	$4\pi h \times 2h \times 4\pi h/3$	$24 \times 64 \times 16$	94	1.1–11	47	-
no-model180MR	180	$4\pi h \times 2h \times 4\pi h/3$	$48 \times 64 \times 32$	47	1.1–11	24	-
no-model180HR	180	$4\pi h \times 2h \times 4\pi h/3$	$96 \times 64 \times 64$	24	1.1–11	12	-
DNS	180	$4\pi h \times 2h \times 4\pi h/3$	$256 \times 128 \times 256$	8.8	0.23–6.8	2.9	-
IA1000VLR	1000	$2\pi h \times 2h \times \pi h$	$48 \times 96 \times 32$	130	1.0–58	98	0.075
IA1000LR	1000	$2\pi h \times 2h \times \pi h$	$96 \times 96 \times 64$	65	1.0–58	49	0.075
IA-LN1000LR	1000	$2\pi h \times 2h \times \pi h$	$96 \times 96 \times 64$	65	1.0–58	49	0.075
DSM1000LR	1000	$2\pi h \times 2h \times \pi h$	$96 \times 96 \times 64$	65	1.0–58	49	-
no-model1000LR	1000	$2\pi h \times 2h \times \pi h$	$96 \times 96 \times 64$	65	1.0–58	49	-

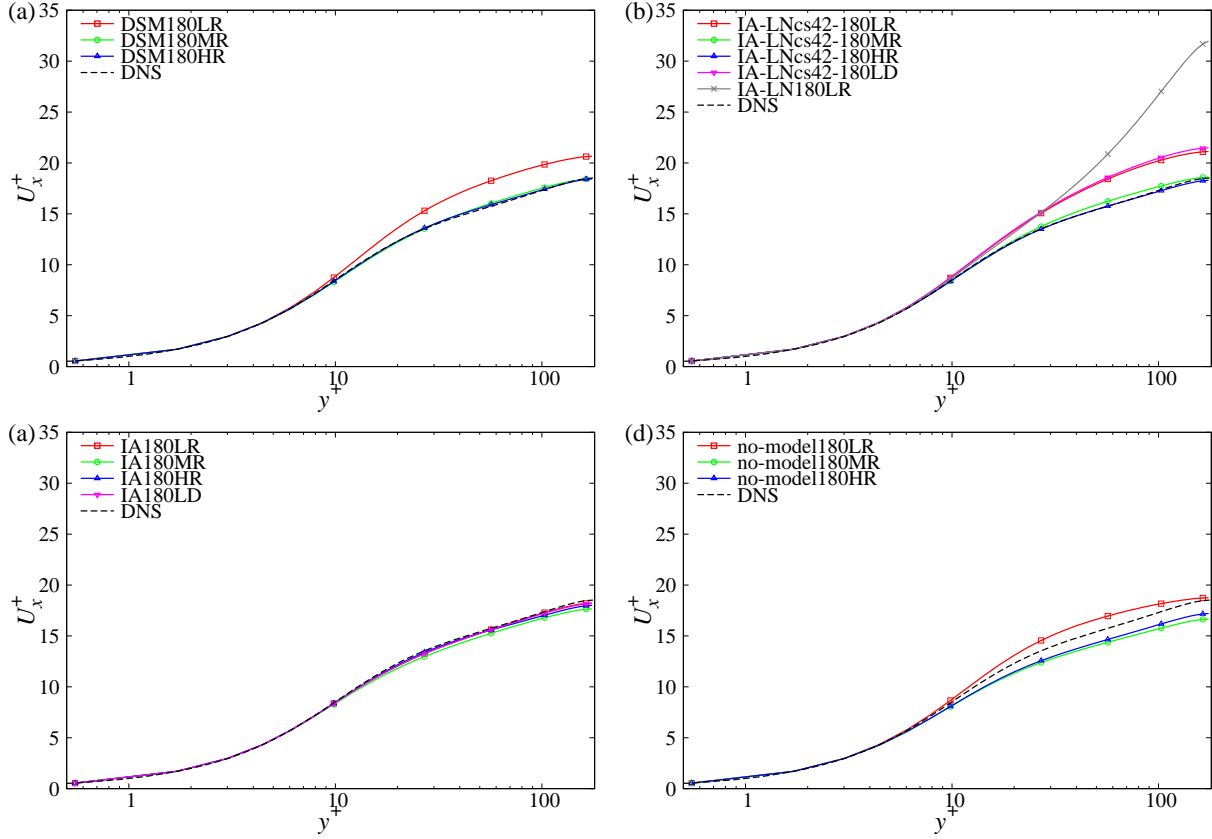


FIG. 1. Mean velocity profile for (a) DSM, (b) IA-LN, (c) IA, and (d) no-model at various resolutions or domain sizes for $Re_\tau = 180$.

lead to a laminar or parabolic profile because the SGS eddy viscosity ν^{sgs} does not vanish due to the mean value of k^{sgs} . Overestimation of the mean velocity is also observed in other eddy-viscosity models^{35,36}. Hence, the EAT makes IA insensitive to the grid resolution. The results in LD overlap those in LR for IA and IA-LNcs42 almost perfectly, which suggests that the statistics of the present simulation depend not on the domain size, but the grid resolution.

Figure 2 shows the mean velocity profile for representative cases at $Re_\tau = 1000$. The reference DNS was performed by Lee and Moser⁵². IA yields a good prediction, while other cases result in overestimation. Surprisingly, IA yields a reasonable prediction even in VLR, where the spanwise grid size is $\Delta z^+ = 98$, which is close to the distance between the streak structure observed in the near-wall region in wall-bounded turbulent flows⁵³. Notably, IA succeeds in predicting the mean velocity profile in the near-wall region $y^+ < 100$, irrespective of the grid resolution. These results suggest that the physical feature of the SMM lies in the near-wall region.

Figure 3 shows the bulk mean velocity normalized by the DNS value for representative cases

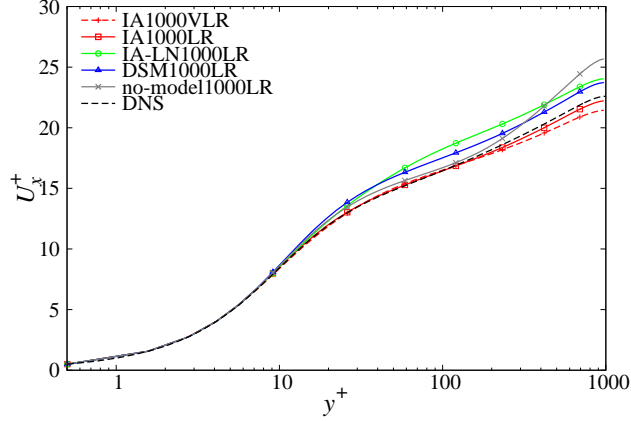


FIG. 2. Mean velocity profile for representative cases at $Re_\tau = 1000$.

with respect to the spanwise grid size. The bulk mean velocity is defined by

$$U_m = \frac{1}{2} \int_0^{2h} dy U_x(y), \quad (20)$$

where $y = 0, 2h$ corresponds to the solid wall boundary. Figure 3 indicates that IA is the least sensitive to the grid resolution, and the error is within 5% for both Reynolds numbers. Interestingly, the no-model overestimates the mean velocity in LR at $Re_\tau = 180$, while it results in underestimation in MR and HR, as observed in Fig. 1(d) and 3. This suggests that the mechanism producing the turbulent momentum transfer or the Reynolds shear stress alters between LR and MR at $Re_\tau = 180$. Generally, insufficient grid resolution without the use of any SGS model makes the system less dissipative, leading to the increase in velocity fluctuations. Consequently, the mean velocity is decreased due to the excessive turbulent momentum transfer. In contrast, in LR, the lack of grid resolution may result in the loss of a generation mechanism of the turbulent or Reynolds shear stress, leading to overestimation of the mean velocity. Considering this situation, it is worth noting that IA succeeds in reproducing the effective momentum transfer due to turbulence even in LR at $Re_\tau = 180$. Therefore, we focus on the properties of models in LR at $Re_\tau = 180$.

2. Mean velocity for various SMMs

Figure 4 shows the mean velocity profile for variable stabilized mixed models including the no EAT model (IA-LNcs42) in LR. The excessive overestimation of IA-ML results from the vanishing GS velocity fluctuations, similar to that shown with IA-LN180LR in Fig. 1(c). The reason behind the failure of IA-ML may be attributed to the scale-similarity model for the SGS-Reynolds term

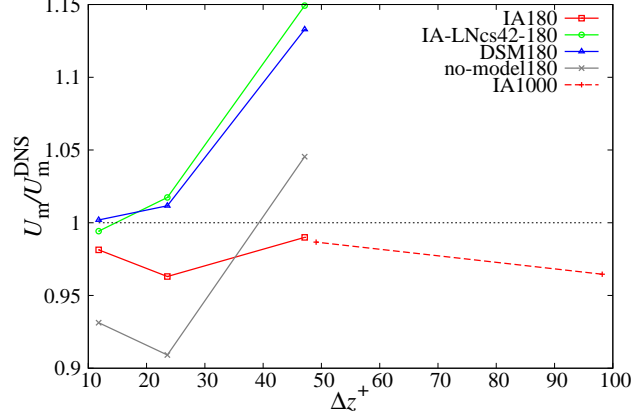


FIG. 3. Bulk mean velocity normalized by DNS value for representative cases with respect to spanwise grid size.

entering the modified Leonard term involves with a negative coefficient, as seen in Eqs. (8) and (10). As both IA and IA-CL yield a reduction of the flow rate compared with other models, the Clark and the SGS-Reynolds terms have similar effect. Moreover, $\bar{\Delta}_i$ is large in LR. Thereby, the first and second terms on the first line of Eq. (8) are canceled each other in the modified Leonard term, yielding the weak contribution of the EAT to the SGS stress for IA-ML. Then, IA-ML leads to a laminarization due to the strong eddy viscosity, as shown in Fig. 1(b). IA-LNcs42 and IA-LV overestimate the mean velocity, while IA-CL underestimates it. The prediction of the mean velocity can be refined by tuning model parameters, e.g., C_{sgs} . However, this is beyond of scope of the present study. A notable point is that IA-CL and IA-LV succeed in sustaining the turbulence even in LR, where it leads to laminarization without the EAT. IA-LV cannot provide a good prediction of the mean velocity, even though the rank of the spatial derivative is the same as the scale-similarity model for the SGS-Reynolds term. Under the scale-similarity assumption, $\bar{u}_i - \widehat{u}_i$ is evaluated as

$$\begin{aligned}
& \bar{u}_i^{(I,J,K)} - \widehat{u}_i^{(I,J,K)} \\
&= \frac{1}{8} \left[\left(\bar{u}_i^{(I-1,J,K)} - 2\bar{u}_i^{(I,J,K)} + \bar{u}_i^{(I+1,J,K)} \right) \right. \\
&\quad + \Delta y^{(J)} \left(-\frac{\bar{u}_i^{(I,J-1,K)} + \bar{u}_i^{(I,J,K)}}{\Delta y^{(J-1/2)}} \right. \\
&\quad\quad\quad \left. \left. + \frac{-\bar{u}_i^{(I,J,K)} + \bar{u}_i^{(I,J+1,K)}}{\Delta y^{(J+1/2)}} \right) \right. \\
&\quad \left. + \left(\bar{u}_i^{(I,J,K-1)} - 2\bar{u}_i^{(I,J,K)} + \bar{u}_i^{(I,J,K+1)} \right) \right], \tag{21}
\end{aligned}$$

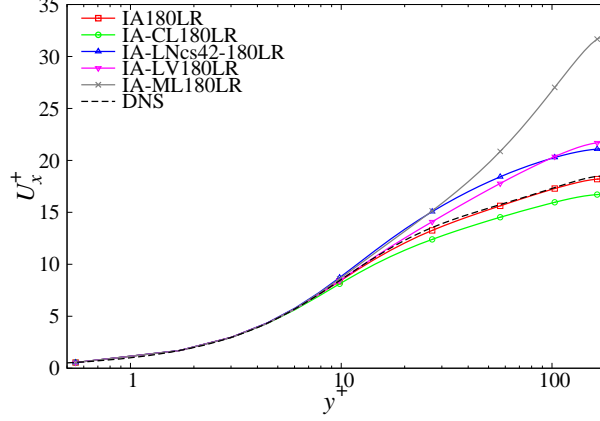


FIG. 4. Mean velocity profile for various SMMs in LR at $Re_\tau = 180$.

while the Laplacian of the velocity for the finite difference with second-order accuracy yields

$$\begin{aligned}
& \nabla^2 \bar{u}_i^{(I,J,K)} \\
&= \frac{1}{(\Delta y^{(J)})^2} \left[\left(\frac{\Delta y}{\Delta x} \right)^2 \left(\bar{u}_i^{(I-1,J,K)} - 2\bar{u}_i^{(I,J,K)} + \bar{u}_i^{(I+1,J,K)} \right) \right. \\
&\quad + \Delta y^{(J)} \left(-\frac{\bar{u}_i^{(I,J-1,K)} + \bar{u}_i^{(I,J,K)}}{\Delta y^{(J-1/2)}} \right. \\
&\quad \quad \left. \left. + \frac{\bar{u}_i^{(I,J,K)} + \bar{u}_i^{(I,J+1,K)}}{\Delta y^{(J+1/2)}} \right) \right. \\
&\quad \left. + \left(\frac{\Delta y}{\Delta z} \right)^2 \left(\bar{u}_i^{(I,J,K-1)} - 2\bar{u}_i^{(I,J,K)} + \bar{u}_i^{(I,J,K+1)} \right) \right]. \quad (22)
\end{aligned}$$

Note that the SMM does not depend on the coefficient $1/(\Delta y^{(J)})^2$, because the EAT is expressed by the form of the normalized tensor. In the present simulation, Δx and Δz are at least about 5 to 10 times larger than Δy . Hence, the x - and z -derivative parts in Eq. (22) contributes little to the EAT. This represents a critical difference between IA and IA-LV. We confirm that the result does not change for IA when the test filter is adopted only to the x and z directions (not shown). Namely, the test filter in the x and z directions is essential in the scale-similarity model for the SGS-Reynolds term in turbulent channel flows.

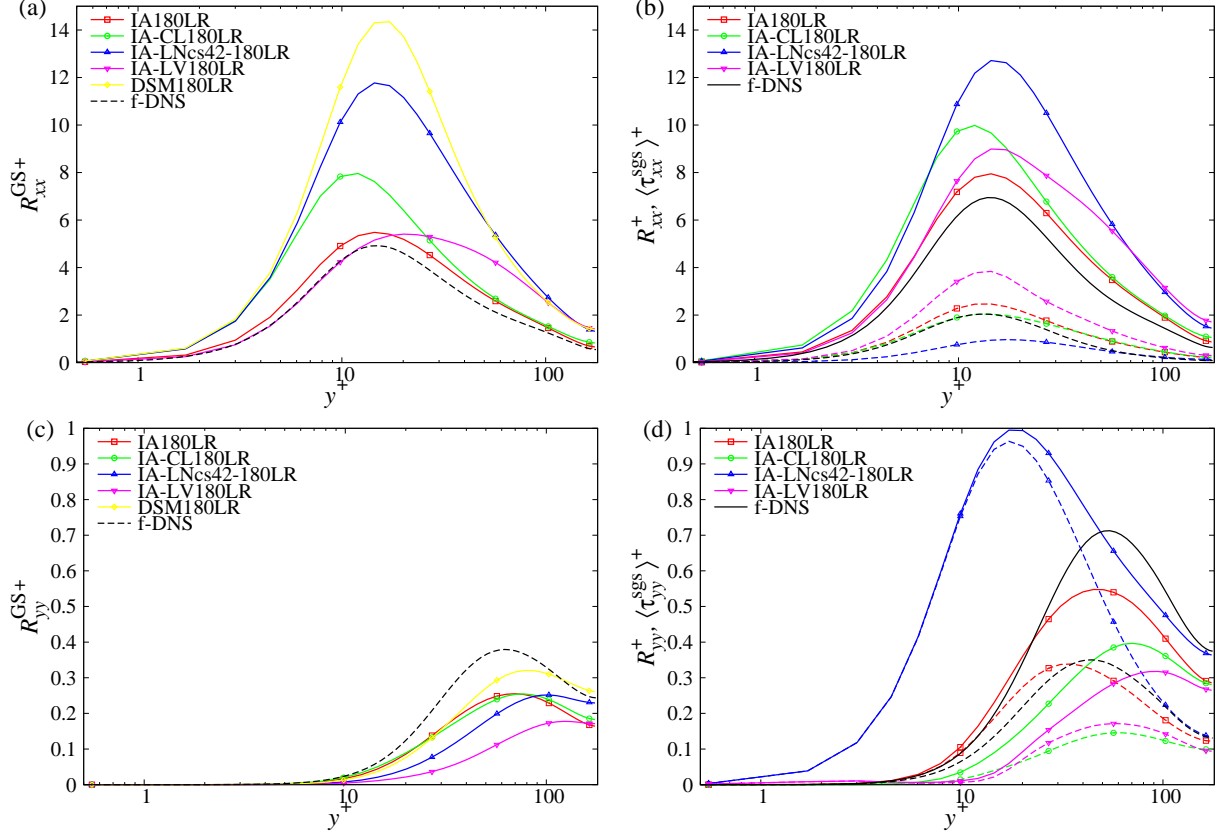


FIG. 5. Profiles of the Reynolds stress of (a) R_{xx}^{GS} , (b) R_{xx} and $\langle \tau_{xx}^{sgs} \rangle^+$, (c) R_{yy}^{GS} , and (d) R_{yy} and $\langle \tau_{yy}^{sgs} \rangle^+$ at $Re_\tau = 180$. In (b) and (d), solid lines depict the total value, while dashed lines depict the SGS value.

3. Reynolds stress

In LES, the Reynolds stress R_{ij} can be defined by

$$R_{ij} = R_{ij}^{GS} + \langle \tau_{ij}^{sgs} \rangle, \quad R_{ij}^{GS} = \langle \overline{u'_i u'_j} \rangle, \quad (23)$$

where $q' (= q - \langle q \rangle)$ is the fluctuation of q around the mean value. For the present SMM, we explicitly solve the SGS kinetic energy k^{sgs} . Thereby, we can calculate the SGS part of the Reynolds stress, which involves k^{sgs} as the isotropic part. Figure 5 shows the profile of the streamwise and wall-normal components of the Reynolds stress for various SMMs in LR at $Re_\tau = 180$. The result for the filtered DNS is likewise plotted, and it is denoted by f-DNS. For DSM, we obtain only the GS value, which is plotted in Fig. 5(a) and (c).

In Fig. 5(a), DSM and IA-LNcs42 overestimate the streamwise component of the GS Reynolds stress R_{xx}^{GS} , which is twice as large as that of f-DNS. R_{xx}^{GS} contributes the most to the GS turbulent kinetic energy $K^{GS} (= R_{ii}^{GS}/2)$ in turbulent channel flows. Such overestimation of the GS turbu-

lent energy is often observed in the LES with coarse grid resolutions (see, e.g., Morinishi and Vasilyev²⁶). IA predicts R_{xx}^{GS} better than other models. Although IA-CL succeeds in reducing R_{xx}^{GS} , it still results in overestimation. IA-LV overestimates R_{xx}^{GS} for $y^+ > 20$. Interestingly, IA-CL overestimates R_{xx}^{GS} , while it underestimates the mean velocity, as shown in Fig. 4. This suggests that the overestimation of R_{xx}^{GS} is not necessarily caused by the overestimation of the velocity gradient. The overestimation of R_{xx}^{GS} leads to overestimation of the total Reynolds stress R_{xx} . In Fig. 5(b), IA gives a reasonable prediction of the total value R_{xx} , while all other models overestimate this value. IA and IA-CL provide a reasonable prediction of the SGS component $\langle \tau_{xx}^{\text{SGS}} \rangle$. IA-LNcs42 underestimates $\langle \tau_{xx}^{\text{SGS}} \rangle$, whereas IA-LV overestimates it. Note that the eddy-viscosity part in the SGS stress contributes little to the normal stress; namely, $\langle \tau_{\alpha\alpha}^{\text{eat}} \rangle \gg -2\langle \mathbf{v}^{\text{SGS}} \bar{s}_{\alpha\alpha} \rangle \simeq 0$ (see, Appendix A). This is in agreement with the statement that the eddy-viscosity model is an ‘isotropic’ model. Thus, we can recognize that the non-eddy-viscosity term is required to express the anisotropy of the SGS stress in turbulent flows.

For R_{yy}^{GS} in Fig. 5(c), DSM seems to provide the best prediction; however, it overestimates R_{xx}^{GS} . Namely, DSM is more anisotropic than f-DNS. IA-LNcs42 is likewise excessively anisotropic. In the present cases, IA yields a good prediction of the wall-normal component of the GS Reynolds stress R_{yy}^{GS} while also efficiently predicting the streamwise component R_{xx}^{GS} . In Fig. 5(d), IA-LNcs42 provides the profile of R_{yy} or $\langle \tau_{yy}^{\text{SGS}} \rangle$ far from f-DNS. As presented in Appendix A, the eddy-viscosity part in the SGS stress contributes little to the normal stress, such that $\langle \tau_{yy}^{\text{SGS}} \rangle \simeq 2\langle k^{\text{SGS}} \rangle / 3$ in IA-LNcs42. For IA, IA-CL, and IA-LV, the wall-normal component of the EAT is negative, i.e., $\langle \tau_{yy}^{\text{eat}} \rangle < 0$. Hence, these SMMs predict a smaller value of the wall-normal Reynolds stress compared with the eddy-viscosity models. In Fig. 5(d), IA seems to yield the best prediction, although it underestimates the GS and the total value of the wall-normal stress.

Figure 6 shows the profiles of the Reynolds shear stress for various cases in LR at $\text{Re}_\tau = 180$. The contribution from the eddy-viscosity term is plotted in Fig. 6(b). For f-DNS, the SGS eddy viscosity \mathbf{v}^{SGS} is evaluated through

$$\mathbf{v}^{\text{SGS}} = -\frac{\tau_{ij}^{\text{SGS}} \bar{s}_{ij}}{2\bar{s}_{\ell m} \bar{s}_{\ell m}}, \quad (24)$$

which is the same approach used in Abe⁴⁰. Note that \mathbf{v}^{SGS} given by Eq. (24) is not necessarily positive. Hence, it allows the backscatter through the eddy-viscosity term, while \mathbf{v}^{SGS} in the present LES is established to be positive. Although this is not a unique approach to determine \mathbf{v}^{SGS} , we can decompose the SGS stress into two parts through this procedure, where one plays the role of

energy transfer between GS and SGS components through the eddy viscosity ν^{sgs} , the other plays the role of SGS forcing apart from the energy transfer. This decomposition is consistent with the concept of the SMM described in Sec. II B.

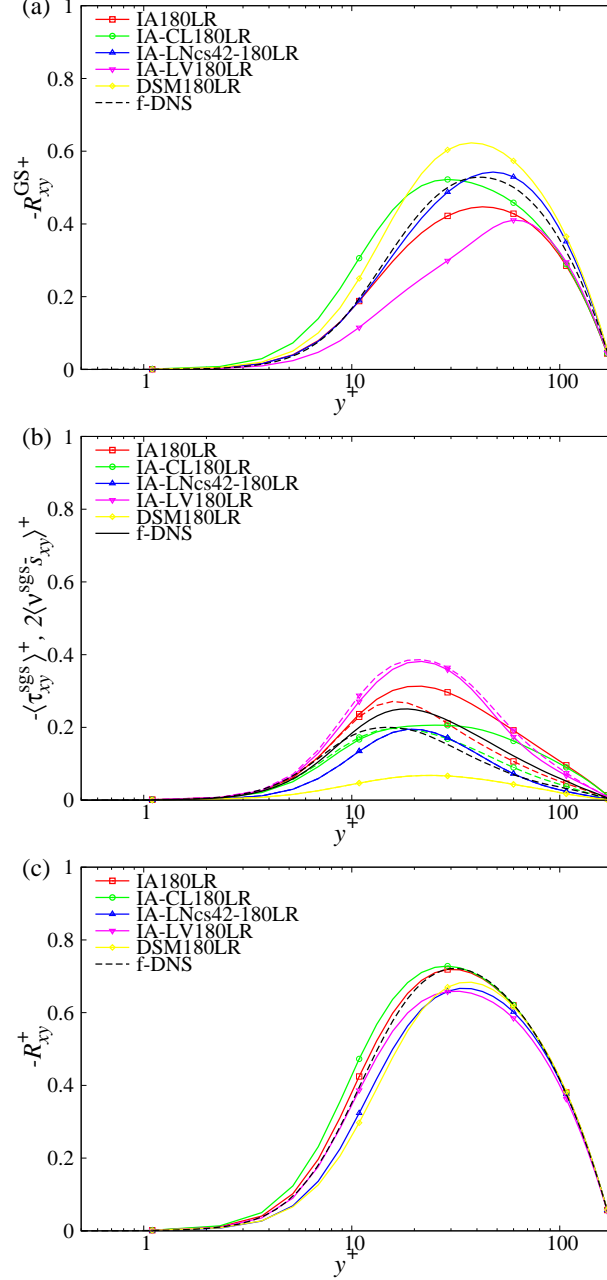


FIG. 6. Profiles of the Reynolds shear stress for (a) GS $-R_{xy}^{\text{GS}}$, (b) SGS $-\langle \tau_{xy}^{\text{sgs}} \rangle$, and (c) total components $-R_{xy}$ at $\text{Re}_\tau = 180$. In (b), solid lines depict the value of $-\langle \tau_{xy}^{\text{sgs}} \rangle$, while dashed lines depict the contribution from the eddy-viscosity term $2\langle \nu^{\text{sgs}} \bar{s}_{xy} \rangle$.

In Fig. 6(a), DSM overestimates the GS component R_{xy}^{GS} . IA-CL and IA-LNcs42 efficiently

predict R_{xy}^{GS} , whereas they overestimate the streamwise velocity fluctuation R_{xx}^{GS} in the same manner as DSM. This suggests that the statistical profiles of the mean velocity and the GS Reynolds shear stress alone cannot account for the overestimation of R_{xx}^{GS} observed in Fig. 5(a), indicating the presence of some effect related to turbulent structures. We discuss this issue further in Sec. IV. IA and IA-LV underestimate R_{xy}^{GS} ; however, IA complements the underestimation of the GS value with the contribution from the SGS part as shown in Fig. 6(c). In Fig. 6(b), we find that the eddy-viscosity term contributes significantly to the SGS shear stress in f-DNS. IA and IA-CL reproduce this trend. In this sense, the value of the eddy-viscosity coefficient $C_{\text{sgs}} = 0.075$ may not be considered an artificially large value, although it is too large to sustain the turbulent fluctuation without the EAT as observed in Fig. 1(b). In Fig. 6(c), IA yields the best prediction of the total Reynolds shear stress R_{xy} , leading to the best prediction of the mean velocity, as shown in Figs. 1 and 4. For IA-CL, the overestimation of $-R_{xy}$ in the near-wall region $y^+ < 30$ results in the underestimation of the mean velocity, as shown in Fig. 4.

4. Lumley's invariant map

To quantitatively evaluate the anisotropy of the turbulent stress for various models, we investigate Lumley's invariant map (see, e.g., Hanjalić and Launder⁴²). We define the GS and SGS normalized anisotropy tensor b_{ij}^{GS} and b_{ij}^{SGS} , respectively, by

$$b_{ij}^{\text{GS}} = \frac{R_{ij}^{\text{GS}}}{R_{\ell\ell}^{\text{GS}}} - \frac{1}{3}\delta_{ij}, \quad b_{ij}^{\text{SGS}} = \frac{\langle \tau_{ij}^{\text{sgs}} \rangle}{\langle \tau_{\ell\ell}^{\text{sgs}} \rangle} - \frac{1}{3}\delta_{ij}. \quad (25)$$

Their second and third invariants read

$$II_b^{\text{A}} = b_{ij}^{\text{A}}b_{ij}^{\text{A}}/2, \quad III_b^{\text{A}} = b_{ij}^{\text{A}}b_{jl}^{\text{A}}b_{li}^{\text{A}}/3, \quad (26)$$

where $\text{A} = \text{GS}, \text{SGS}$. The realizability conditions^{54,55} for the Reynolds or SGS stress indicate that the invariants (26) lie in the following region⁴²:

$$II_b^{\text{A}} \leq 2III_b^{\text{A}} + \frac{2}{9}, \quad (III_b^{\text{A}})^3 \geq 6(III_b^{\text{A}})^2. \quad (27)$$

Figure 7 shows the invariant map for various cases at $\text{Re}_\tau = 180$. The values for $y^+ < 20$ are plotted with symbols. In this map, the upper line, $II_b^{\text{A}} = 2III_b^{\text{A}} + 2/9$, denotes the two-component turbulence. In turbulent channel flows, this corresponds to the condition that the wall-normal stress is negligible relative to the streamwise and spanwise components. The upper right tip corresponds to

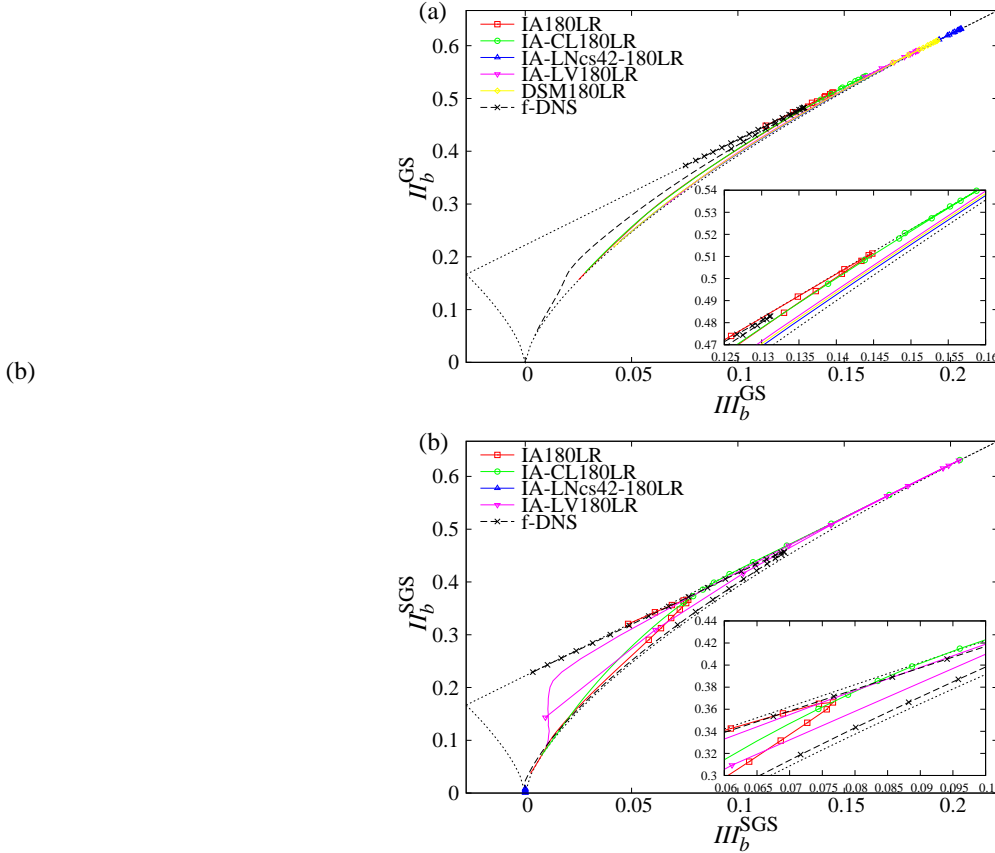


FIG. 7. Lumley’s invariant map for (a) GS and (b) SGS normalized anisotropy tensor at $Re_\tau = 180$. Values for $y^+ < 20$ are plotted with symbols. The inset shows the enlarged view in which IA turns around. The channel center corresponds to the end of lines closest to the origin. As it approaches the solid wall, f-DNS proceeds toward the right top, then turns around and asymptotically approaches the top line of the two-component turbulence, in both (a) and (b).

the one-component turbulence (only the streamwise component), whereas the left tip corresponds to the two-component isotropic turbulence. The origin is the three-component isotropic condition.

In Fig. 7(a), IA-LNcs42, IA-LV, and DSM approach the top right tip as they proceed toward the solid wall, which indicates that the GS velocity fluctuation becomes nearly one component. The profiles for IA-CL and IA approach that for f-DNS; namely, they recover the asymptotic behavior of the GS turbulence anisotropy in the vicinity of the wall. The anisotropy of the SGS component exhibit more evident differences between the models than the GS component. In Fig. 7(b), it should be noted that IA-LNcs42 lies at the origin, which indicates that the SGS stress is isotropic. This reflects the property of the eddy-viscosity model as the ‘isotropic’ model. IA-LV exhibits strange behavior, and it does not asymptotically approach the two-component turbulence in the

vicinity of the wall. This is because IA-LV fails to reproduce the asymptotics of the wall-normal stress, $\langle \tau_{yy}^{\text{SGS}} \rangle \sim O(y^4)$. IA-CL approaches the two-component turbulence in the vicinity of the wall; however it approaches the one-component turbulence tip and does not turn around. Only IA turns around in the near-wall region, such that it reproduces the asymptotic trend of the SGS stress in the vicinity of the wall, although it does not perfectly correspond to f-DNS. In summary, IA yields the best prediction among the presented models on the anisotropy of both the GS and SGS stress.

5. Reynolds stress spectrum

According to Abe⁴⁰, the SMM employing the scale-similarity model for the SGS-Reynolds term recovers the energy spectrum close to the cut-off scale. The energy spectrum reflects information concerning turbulent structures such as streak structures observed in wall-bounded turbulence. We define the spectrum of the GS Reynolds stress by

$$E_{ij}^{\text{GS}}(k_x, y, k_z) = \Re \langle \tilde{u}_i \tilde{u}_j^* \rangle, \quad (28)$$

$$R_{ij}^{\text{GS}}(y) = \sum_{k_x=0}^{k_x^{\max}} \sum_{k_z=0}^{k_z^{\max}} E_{ij}^{\text{GS}}(k_x, y, k_z) \Delta k_x \Delta k_z, \quad (29)$$

where $k_\alpha^{\max} = \pi N_\alpha / L_\alpha$, $\Delta k_\alpha = 2\pi / L_\alpha$, $\alpha = x, z$, the superscript ‘*’ denotes the complex conjugate, and $\tilde{q}^{(J)}$ is the Fourier coefficient of an instantaneous variable q , defined by

$$\tilde{q}^{(J)}(k_x, k_z) = \frac{1}{N_x N_z} \sum_{I=1}^{N_x} \sum_{K=1}^{N_z} q^{(I,J,K)} e^{-i(k_x I L_x / N_x + k_z K L_z / N_z)}. \quad (30)$$

Hereafter, we focus on the streamwise spectrum $E_{ij}^{\text{GS}}(k_x, y)$, which is defined by

$$E_{ij}^{\text{GS}}(k_x, y) = \sum_{k_z=0}^{k_z^{\max}} E_{ij}^{\text{GS}}(k_x, y, k_z) \Delta k_z \quad (31)$$

Because the difference between the models is evident at $y^+ = 20$ for both the mean velocity in Fig. 4 and the Reynolds stress in Figs. 5 and 6, we focus on the spectrum at that plane.

Figure 8 shows the streamwise spectrum of the GS Reynolds stress for various cases in LR or LD at $y^+ = 20$ for $\text{Re}_\tau = 180$. We plot the result for the non-filtered DNS for reference. To emphasize the high-wavenumber or low-wavelength region, we set the horizontal axis in the wavelength $\lambda_x (= 2\pi/k_x)$ instead of the wavenumber k_x . First, the results in LD almost overlap

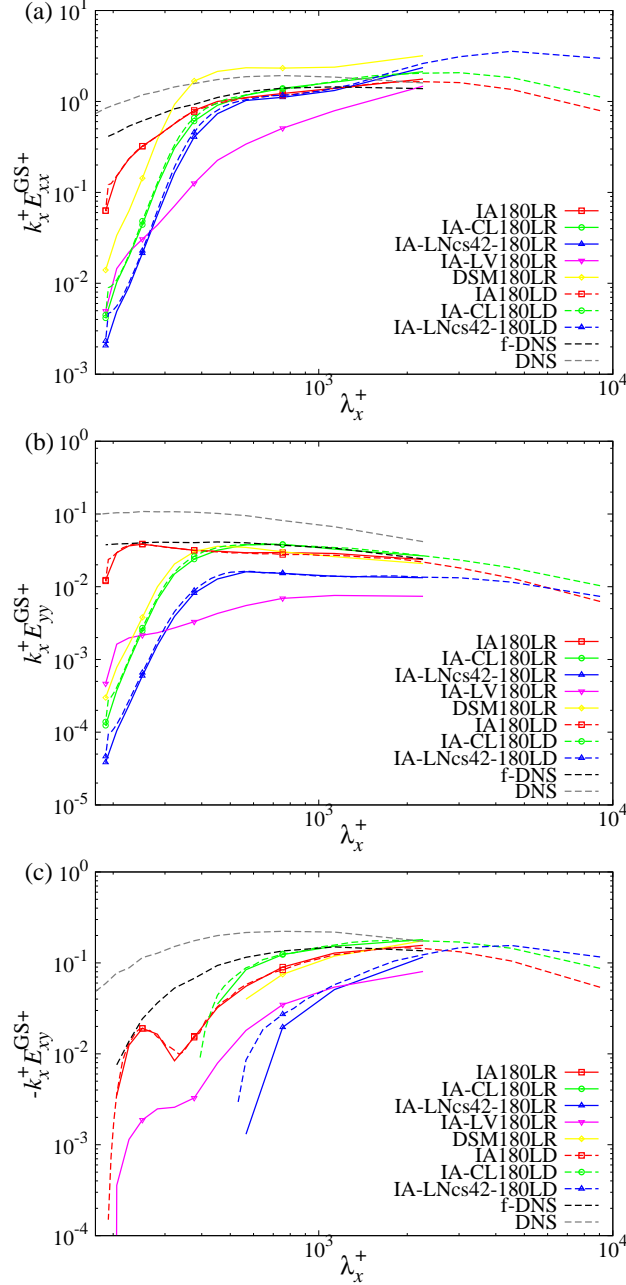


FIG. 8. Profiles of the GS Reynolds stress spectrum for (a) streamwise E_{xx}^{GS} , (b) wall-normal E_{yy}^{GS} , and (c) shear components $-E_{xy}^{\text{GS}}$ at $y^+ = 20$ for $\text{Re}_\tau = 180$.

those in LR, in the same manner as the mean velocity in Fig. 1. Hence, the statistics in the present LES do not depend on the domain size, but on the grid resolution. In Fig. 8(a), as shown by Abe⁴⁰, IA recovers the intensity of the GS streamwise velocity spectrum close to the cut-off wavelength scale. The spectrum of the GS streamwise velocity is related to the near-wall streak structure. The spectrum accumulated in the high-wavelength region such as IA-LNcs42 or DSM, indicates that

the structure elongated in the streamwise direction is considerably more dominant than the short scale structures. For IA-CL, the slope of the spectrum at the high-wavelength region is gentle. This indicates that IA-CL succeeds in reproducing the length of the streak structure to some extent. This is further discussed in Sec. IV B. Several studies discussed the relation between the breakdown of the streaks and the sustaining process of turbulent shear flows^{56,57}. In this sense, IA may succeed in reproducing the sustaining process of turbulent shear flow with the coarse grid by the enhancement of the turbulence close to the cut-off scale. As shown in Fig. 8(b), IA also predicts the GS wall-normal velocity spectrum in the entire wavelength range. Other models, including IA-CL, cannot reproduce the spectrum close to the cut-off wavelength scale. The difference between IA and IA-CL suggests that the EAT, based not on the first-order but on the second-order spatial derivative of the velocity field, is useful in restoring the behavior of the spectra close to the cut-off scale.

For E_{xy}^{GS} in Fig. 8(c), the lines disappear at the low-wavelength region for some models. This is because $-E_{xy}^{\text{GS}}$ is negative at wavelength regions below that scale. In contrast, IA predicts the positive $-E_{xy}^{\text{GS}}$ up to the cut-off wavelength as efficiently as f-DNS. Although IA-LV likewise predicts a positive $-E_{xy}^{\text{GS}}$ value in the entire wavelength region, the value is smaller than that obtained by IA or f-DNS. Furthermore, IA-LV cannot predict E_{xx}^{GS} and E_{yy}^{GS} at the low-wavelength region. For IA in Fig. 8(c), the spectrum bends around $\lambda_x^+ = 300$. This corresponds to the contribution of the EAT on the budget of E_{yy}^{GS} , as described later in Sec. IV A 2. However, the success of IA suggests that the reproduction of the GS Reynolds shear stress spectrum E_{xy}^{GS} close to the cut-off scale is an essence of further development of SGS models.

IV. DISCUSSION

A. Budget equation for the GS Reynolds stress spectrum

As shown in Sec. III, the SGS models showed evident differences on anisotropy and structures represented by the Reynolds stress spectrum, in the near-wall region. To investigate the effect of the SGS stress on both anisotropy and structures of turbulence in shear flows, it is useful to analyze the budget equation for the Reynolds stress spectrum⁴³⁻⁴⁵. In the use of SGS models, the budget equation for the GS Reynolds stress spectrum yields

$$\frac{\partial E_{ij}^{\text{GS}}}{\partial t} + \frac{\partial}{\partial x_\ell} (U_\ell E_{ij}^{\text{GS}})$$

$$\begin{aligned}
&= \check{P}_{ij}^{\text{GS}} - \check{\xi}_{ij}^{\text{GS}} + \check{D}_{ij}^{\text{t,GS}} + \check{\Phi}_{ij}^{\text{GS}} + \check{D}_{ij}^{\text{p,GS}} + \check{D}_{ij}^{\text{v,GS}} + \check{T}_{ij}^{\text{GS}} \\
&\quad + \check{\xi}_{ij}^{\text{SGS}} + \check{D}_{ij}^{\text{SGS}}.
\end{aligned} \tag{32}$$

Each term on the right-hand side is referred to as the production $\check{P}_{ij}^{\text{GS}}$, destruction $\check{\xi}_{ij}^{\text{GS}}$, turbulent diffusion $\check{D}_{ij}^{\text{t,GS}}$, pressure–strain correlation $\check{\Phi}_{ij}^{\text{GS}}$, pressure diffusion $\check{D}_{ij}^{\text{p,GS}}$, viscous diffusion $\check{D}_{ij}^{\text{v,GS}}$, inter-scale transfer $\check{T}_{ij}^{\text{GS}}$, SGS destruction $\check{\xi}_{ij}^{\text{SGS}}$, and SGS diffusion $\check{D}_{ij}^{\text{SGS}}$, respectively. When the turbulent field is inhomogeneous only in the y direction, they are defined as follows:

$$\check{P}_{ij}^{\text{GS}} = -E_{iy}^{\text{GS}} \frac{\partial U_j}{\partial y} - E_{jy}^{\text{GS}} \frac{\partial U_i}{\partial y}, \tag{33a}$$

$$\check{\xi}_{ij}^{\text{GS}} = 2\nu \Re \left\langle \tilde{s}'_{i\ell} (\tilde{\partial}_\ell \tilde{u}'_j)^* + \tilde{s}'_{j\ell} (\tilde{\partial}_\ell \tilde{u}'_i)^* \right\rangle, \tag{33b}$$

$$\check{D}_{ij}^{\text{t,GS}} = -\frac{\partial}{\partial y} \Re \left\langle \tilde{u}'_y (\widetilde{u'_i u'_j})^* \right\rangle, \tag{33c}$$

$$\check{\Phi}_{ij}^{\text{GS}} = 2\Re \left\langle \tilde{p}^{\text{total}/\tilde{s}'_{ij}} \right\rangle, \tag{33d}$$

$$\check{D}_{ij}^{\text{p,GS}} = -\frac{\partial}{\partial y} \left[\Re \left\langle \tilde{p}^{\text{total}/\tilde{u}'_i} \right\rangle \delta_{jy} + \Re \left\langle \tilde{p}^{\text{total}/\tilde{u}'_j} \right\rangle \delta_{iy} \right], \tag{33e}$$

$$\check{D}_{ij}^{\text{v,GS}} = 2\nu \frac{\partial}{\partial y} \Re \left\langle \tilde{s}'_{jy} \tilde{u}'_i + \tilde{s}'_{iy} \tilde{u}'_j \right\rangle, \tag{33f}$$

$$\check{T}_{ij}^{\text{GS}} = \Re \left\langle \tilde{u}'_j \tilde{N}_i + \tilde{u}'_i \tilde{N}_j \right\rangle - \check{P}_{ij}^{\text{GS}} - \check{D}_{ij}^{\text{t,GS}}, \tag{33g}$$

$$\check{\xi}_{ij}^{\text{SGS}} = \Re \left\langle \tilde{\tau}_{i\ell}^{\text{sgs}/\text{tl}} (\tilde{\partial}_\ell \tilde{u}'_j)^* + \tilde{\tau}_{j\ell}^{\text{sgs}/\text{tl}} (\tilde{\partial}_\ell \tilde{u}'_i)^* \right\rangle, \tag{33h}$$

$$\check{D}_{ij}^{\text{SGS}} = -\frac{\partial}{\partial y} \Re \left\langle \tilde{\tau}_{jy}^{\text{sgs}/\text{tl}} \tilde{u}'_i + \tilde{\tau}_{iy}^{\text{sgs}/\text{tl}} \tilde{u}'_j \right\rangle, \tag{33i}$$

where $\tilde{\partial}_j = (ik_x, \partial/\partial y, ik_z)$, and $N_i = -\partial(\bar{u}_i \bar{u}_j)/\partial x_j$. \bar{p}^{total} is the sum of \bar{p} and the SGS dynamic pressure $2k^{\text{sgs}}/3$; namely, it is defined by

$$\bar{p}^{\text{total}} = \bar{p} + \frac{2}{3}k^{\text{sgs}}. \tag{34}$$

Furthermore, we decompose the SGS destruction term into two terms as follows:

$$\check{\xi}_{ij}^{\text{SGS}} = -\check{\xi}_{ij}^{\text{EV}} + \check{\xi}_{ij}^{\text{EAT}}, \tag{35}$$

where

$$\check{\xi}_{ij}^{\text{EV}} = 2\Re \left\langle \widetilde{\mathbf{v}^{\text{sgs}} \tilde{s}'_{i\ell}} (\tilde{\partial}_\ell \tilde{u}'_j)^* + \widetilde{\mathbf{v}^{\text{sgs}} \tilde{s}'_{j\ell}} (\tilde{\partial}_\ell \tilde{u}'_i)^* \right\rangle, \tag{36a}$$

$$\check{\xi}_{ij}^{\text{EAT}} = \Re \left\langle \tilde{\tau}_{i\ell}^{\text{eat}/\text{tl}} (\tilde{\partial}_\ell \tilde{u}'_j)^* + \tilde{\tau}_{j\ell}^{\text{eat}/\text{tl}} (\tilde{\partial}_\ell \tilde{u}'_i)^* \right\rangle, \tag{36b}$$

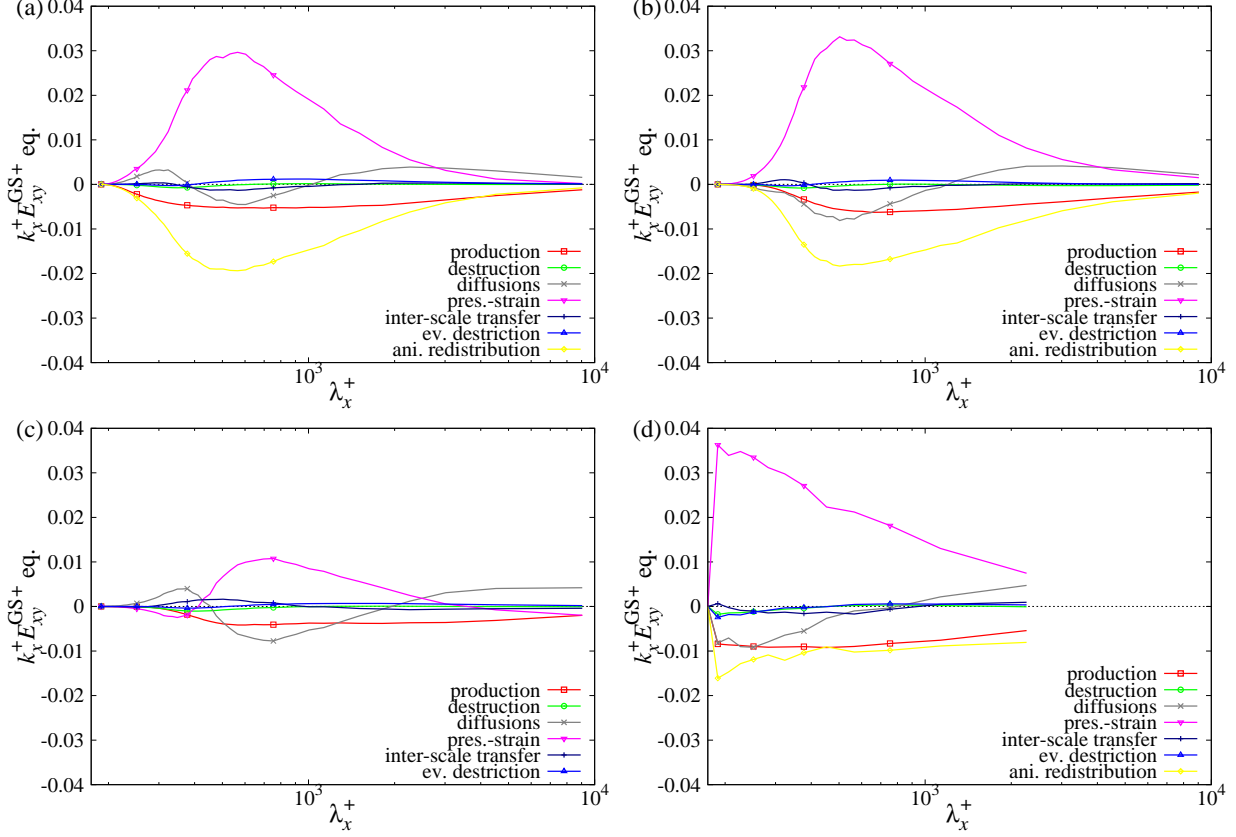


FIG. 9. Budget for the GS Reynolds shear stress spectrum E_{xy}^{GS} normalized by viscous unit for (a) IA180LD, (b) IA-CL180LD, (c) IA-LNcs42-180LD, and (d) f-DNS at $y^+ = 20$ for $\text{Re}_\tau = 180$.

where τ_{ij}^{cat} is defined in Eq. (11). We refer to ξ_{ij}^{EV} and ζ_{ij}^{EAT} as the eddy-viscosity destruction and the anisotropic redistribution terms, respectively. When the budget Eq. (32) is summed over the wavenumbers, it leads to the conventional budget for the GS Reynolds stress (see, Appendix B or Abe⁴⁰):

$$A_{ij}^{\text{GS}} = \sum_{k_x=0}^{k_x^{\text{max}}} \check{A}_{ij}^{\text{GS}} \Delta k_x, \quad (37)$$

where $\check{A}_{ij}^{\text{GS}}$ corresponds to each term in Eq. (33a)–(33i), (36a), and (36b), while A_{ij}^{GS} corresponds to each term on the right-hand side of Eq. (B1).

1. Shear component

A critical feature of the IA model is that it reproduces the positive $-E_{xy}^{\text{GS}}$ in the entire wavelength region, as shown in Fig. 8(c). Abe⁴⁰ showed that the anisotropic redistribution term ζ_{xy}^{EAT} is indispensable to predict the profile of the SGS destruction term obtained from the filtered DNS in

the budget of the GS Reynolds shear stress R_{xy}^{GS} . Figure 9 shows the budget for the GS Reynolds shear stress spectrum E_{xy}^{GS} for representative cases at $y^+ = 20$ for $\text{Re}_\tau = 180$. For all cases, the eddy-viscosity destruction term contributes little to the budget in the entire wavelength region. This is a critical shortcoming of the eddy-viscosity models. IA-LNcs42 fails to predict the profile of the pressure–strain correlation $\check{\Phi}_{xy}^{\text{GS}}$ in Fig. 9(c). IA and IA-CL qualitatively reproduce the profile of the pressure–strain correlation $\check{\Phi}_{xy}^{\text{GS}}$ and anisotropic redistribution $\check{\xi}_{xy}^{\text{EAT}}$ obtained from f-DNS. The difference between IA and IA-CL lies in the profile of the production term $\check{P}_{xy}^{\text{GS}}$. $\check{P}_{xy}^{\text{GS}}$ in IA-CL in Fig. 9(b) disappears close to the cut-off wavelength scale. This arises from the profile of E_{yy}^{GS} , because $\check{P}_{xy}^{\text{GS}}$ reads

$$\check{P}_{xy}^{\text{GS}} = -E_{yy}^{\text{GS}} \frac{\partial U_x}{\partial y}. \quad (38)$$

Hence, the reproduction of $\check{P}_{xy}^{\text{GS}}$ close to the cut-off wavelength scale relies on the reproduction of E_{yy}^{GS} .

2. Wall-normal component

Figure 10 shows the budget for the wall-normal component of the GS Reynolds stress spectrum E_{yy}^{GS} for representative cases at $y^+ = 20$ for $\text{Re}_\tau = 180$. Both IA-CL and IA fail to reproduce the profile of the anisotropic redistribution term $\check{\xi}_{yy}^{\text{EAT}}$ obtained from f-DNS. However, they provide a reasonable prediction of the sum of the pressure–strain correlation and the anisotropic redistribution terms $\check{\Phi}_{yy}^{\text{GS}} + \check{\xi}_{yy}^{\text{EAT}}$. For IA in Fig. 10(a), $\check{\Phi}_{yy}^{\text{GS}} + \check{\xi}_{yy}^{\text{EAT}}$ is positive close to the cut-off wavelength scale, as is the case with f-DNS in Fig. 10(d). Hence, IA succeeds in reproducing the large intensity of the wall-normal component of the Reynolds stress spectrum E_{yy}^{GS} , as shown in Fig. 8(b). For IA in Fig. 10(a), the wavelength in which the anisotropic redistribution term $\check{\xi}_{yy}^{\text{EAT}}$ exhibits a dent corresponds to that in which $-E_{xy}^{\text{GS}}$ is bent in Fig. 8(c). This suggests that the reproduction of the spectrum close to the cut-off scale for the shear component $-E_{xy}^{\text{GS}}$ is realized by the increase of the wall-normal velocity fluctuation at that scale attributed to the EAT through the anisotropic redistribution term $\check{\xi}_{yy}^{\text{EAT}}$.

Figure 11 shows the contour map of the sum of the pressure–strain correlation and the anisotropic redistribution terms $\check{\Phi}_{yy}^{\text{GS}} + \check{\xi}_{yy}^{\text{EAT}}$ in the budget equation for the wall-normal component of the GS Reynolds stress spectrum E_{yy}^{GS} , for representative cases at $y^+ = 20$ for $\text{Re}_\tau = 180$. All cases are similar, except for the region close to the cut-off wavelength scale, where IA exhibits

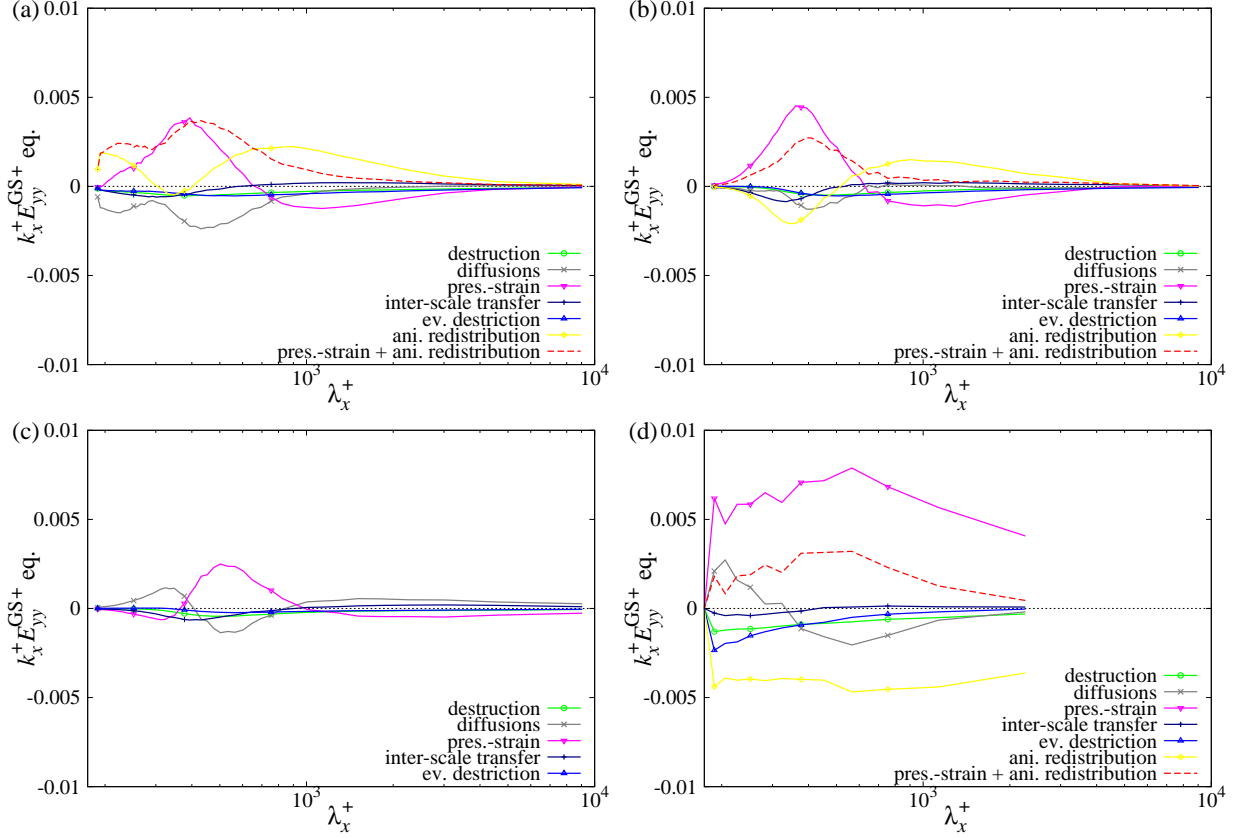


FIG. 10. Budget for the wall-normal component of the GS Reynolds spectrum E_{yy}^{GS} normalized by viscous unit for (a) IA180LD, (b) IA-CL180LD, (c) IA-LNcs42-180LD, and (d) f-DNS at $y^+ = 20$ for $Re_\tau = 180$.

a comparable value to the middle wavelength scale, as is the case with f-DNS. The negative contribution for $y^+ < 10$ corresponds to the ‘splating’ effect^{45,58}, leading to the two-component turbulence, as observed in Fig. 7(a). The positive contribution of $\check{\Phi}_{yy}^{GS} + \check{\xi}_{yy}^{EAT}$ in the region $y^+ > 10$ and $\lambda_x^+ < 300$ for IA in Fig. 11(a) leads to the reproduction of E_{yy}^{GS} close to the cut-off scale, as shown in Fig. 8(b). The reproduction of E_{yy}^{GS} close to the cut-off scale results in feedback to the budget of E_{xy}^{GS} as a source term through the production term \check{P}_{xy}^{GS} .

3. Streamwise component

Figure 12 shows the budget for the streamwise component of the GS Reynolds stress spectrum E_{xx}^{GS} for representative cases at $y^+ = 20$ for $Re_\tau = 180$. The production term \check{P}_{xx}^{GS} for IA in Fig. 12(a) provides a positive value close to the cut-off wavelength scale owing to the reproduction

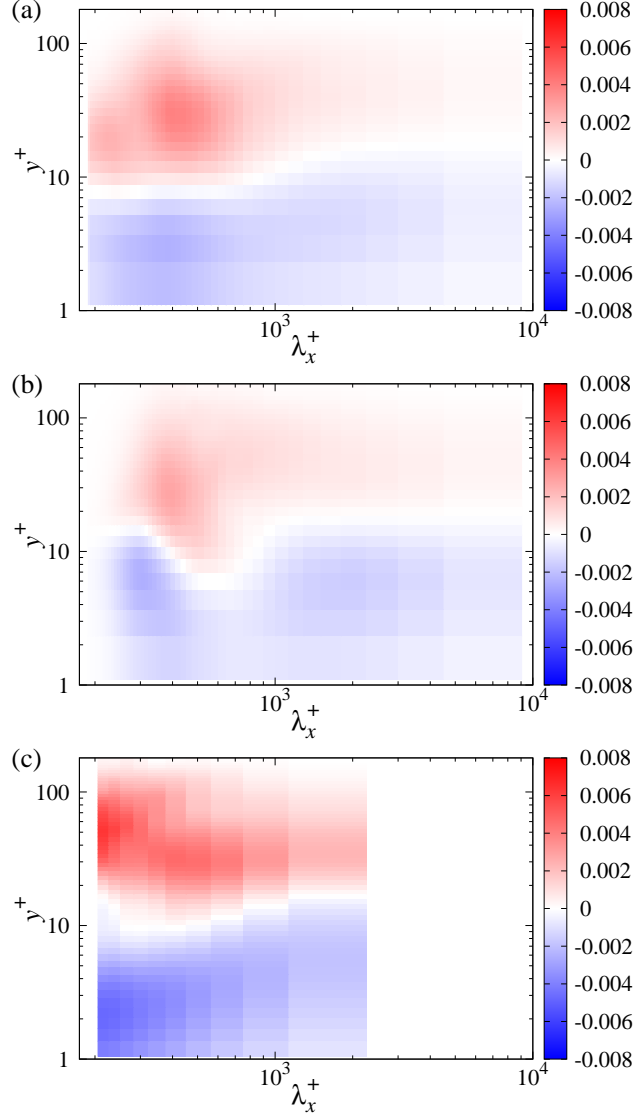


FIG. 11. Contour map of sum of the pressure–strain correlation and the anisotropic redistribution terms $\check{\Phi}_{yy}^{\text{GS}} + \check{\xi}_{yy}^{\text{EAT}}$ in budget for the wall-normal component of the GS Reynolds stress spectrum E_{yy}^{GS} normalized by viscous unit for (a) IA180LD, (b) IA-CL180LD, and (c) f-DNS at $\text{Re}_\tau = 180$.

of E_{xy}^{GS} , because $\check{P}_{xx}^{\text{GS}}$ reads

$$\check{P}_{xx}^{\text{GS}} = -2E_{xy}^{\text{GS}} \frac{\partial U_x}{\partial y}. \quad (39)$$

Moreover, the anisotropic redistribution term $\check{\xi}_{xx}^{\text{EAT}}$ is likewise positive in the entire wavelength range for IA. Although the profiles of each term are different between IA and f-DNS, IA succeeds in enhancing the GS streamwise velocity fluctuation in the low-wavelength region close to the cut-off scale. In contrast, in IA-CL, the anisotropic redistribution term $\check{\xi}_{xx}^{\text{EAT}}$ contributes little to

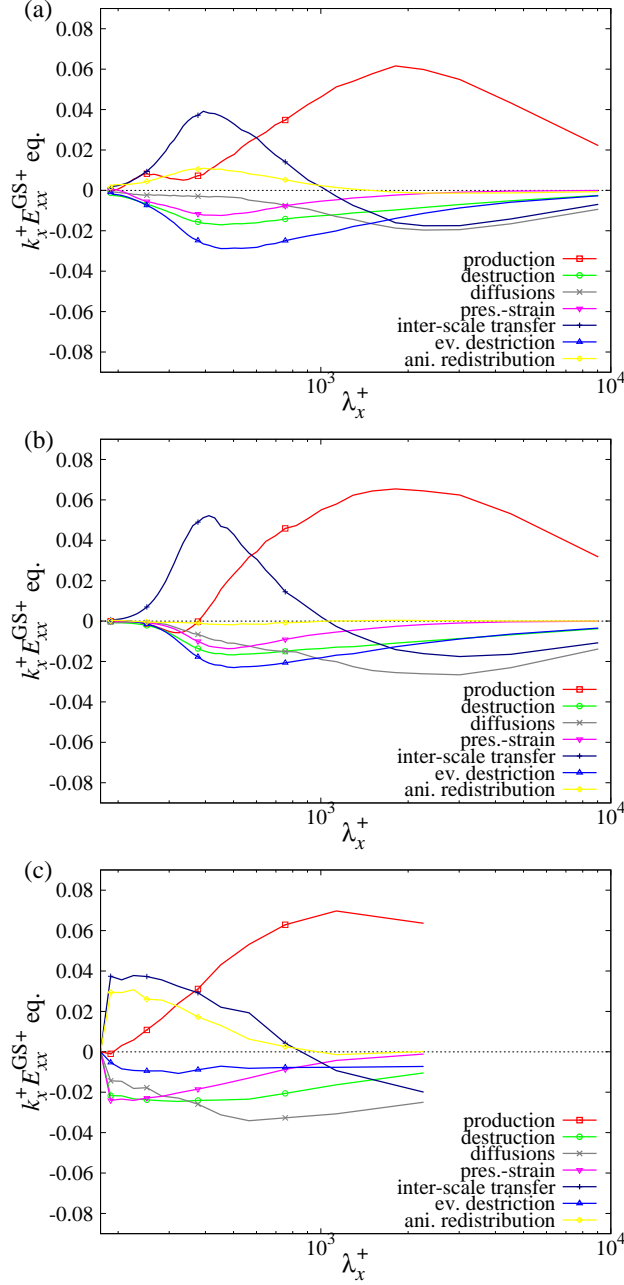


FIG. 12. Budget for the streamwise component of the GS Reynolds spectrum E_{xx}^{GS} normalized by viscous unit for (a) IA180LD, (b) IA-CL180LD, and (c) f-DNS at $y^+ = 20$ for $Re_\tau = 180$

the budget in the entire wavelength range, and the production becomes negative close the cut-off wavelength scale. This leads to the rapid decay of the spectrum in the low-wavelength region, as shown in Fig. 8(a). Furthermore, the increase in the velocity fluctuation in the low-wavelength region leads to the enhancement of the dissipation. In fact, the eddy-viscosity destruction for IA in Fig. 12(a) is larger than that for IA-CL in Fig. 12(b). This accounts for the difference between

the profiles of the GS streamwise velocity fluctuation for IA and IA-CL in Fig. 5(a). Hence, the overestimation of the GS streamwise velocity fluctuation can be restored by the increase of the turbulence close the cut-off wavelength scale.

4. Summary of analysis through budget for the GS Reynolds stress spectrum

We summarize the physical role of the EAT in the SMM in turbulent channel flows. The EAT in IA model enhances the wall-normal component of the velocity fluctuation through the anisotropic redistribution term. This feeds the streamwise and shear components of the GS Reynolds stress in the low-wavelength region close to the cut-off scale, through the production term. Consequently, IA succeeds in activating turbulence in the entire wavelength range. To achieve this activation, the scale-similarity model for the SGS-Reynolds term is more appropriate than the Clark term, as the former is based on a higher-order spatial derivative than the latter. Hence, the scale-similarity model for the SGS-Reynolds term is efficient in enhancing the turbulence close to the cut-off scale.

Anderson and Domaradzki²⁷ discussed the physics of inter-scale energy transfer among the largest, small resolved, and sub-grid scales, through scale-similarity models. They showed that the modified Leonard-like term yields an excessive dissipation directly from the largest resolved scales, which is unphysical in the concept of localness in scale of energy transfer. Such a non-local energy transfer does not occur in the SMM because the energy transfer between the GS and SGS due to the EAT is prohibited, although the EAT can redistribute energy between mean and the GS turbulent kinetic energies, as shown in Appendix B. A failure of IA-CL may be partly attribute to the similar mechanism suggested by Anderson and Domaradzki²⁷, because the Clark term retains only the leading term of the scale-similarity model for the SGS stress, as shown in Eq. (6) and (8). Namely, the Clark term may be dominant in the largest resolved scale, although the statistical contribution of $\check{\xi}_{xx}^{\text{EAT}}$ is negligible, as shown in Figs. 12(b). In contrast, the scale-similarity model for the SGS-Reynolds term (17) is composed only by the small resolved scale velocity, which more correlates to the small resolved scale than the largest scale. This is observed from $\check{\xi}_{xx}^{\text{EAT}}$ in Figs. 12(a). Thereby, IA does not suffer from the non-local property of the scale-similarity model suggested by Anderson and Domaradzki²⁷.

We also investigate the model where the EAT enters with a negative coefficient, $\tau_{ij}^{\text{sgs}}|_{\text{II}} = -2\nu^{\text{sgs}}\bar{s}_{ij} - \tau_{ij}^{\text{eat}}$, through the scale-similarity model for the SGS-Reynolds term, because this term yields a negative correlation on the energy transfer between the GS and SGS fields around an

elliptic Burgers vortex¹⁶. However, this model excessively overestimates the mean velocity (not shown). Moreover, it violates the realizability conditions^{54,55} for the SGS stress, as $\langle \tau_{xx}^{\text{sgs}} \rangle < 0$. This is because it usually yields $\tau_{xx}^a/\tau_{\ell\ell}^a > 2/3$ with Eq. (17) in turbulent channel flows, resulting in $\langle \tau_{xx}^{\text{sgs}} \rangle \simeq \langle 2k^{\text{sgs}}[1/3 - (\tau_{xx}^a/\tau_{\ell\ell}^a - 1/3)] \rangle < 0$. Furthermore, the form of the EAT provided in Eq. (16) is likewise a key element. The present simulation of IA shows that $\langle 2k^{\text{sgs}}/\tau_{\ell\ell}^a \rangle \gg 1$. Hence, the contribution of the scale-similarity model is enhanced as compared with the case when it is simply added. These results suggest that it is not sufficient to simply add the EAT to improve the SGS model. Instead, we should properly express the EAT, which efficiently excites turbulence close to the cut-off scale.

B. Streak structures in stabilized mixed models

As shown in Fig. 8(a), all SGS models except for IA result in the rapid decay of the spectrum of the streamwise turbulent fluctuation in the low-wavelength region. The spectrum accumulated in the high-wavelength region corresponds to the flow structure excessively elongated in the streamwise direction. Figure 13 shows the contour map of the instantaneous streamwise velocity fluctuation $\bar{u}_x - \langle \bar{u}_x \rangle_{x-z\text{-plane}}$ at $y^+ = 20$ for $\text{Re}_\tau = 180$. Figure 13(c) indicates that IA-LNcs42 predicts excessively elongated streamwise streak structures. In Figs. 13(a) and (b), IA and IA-CL predict reasonable streak structures in comparison with f-DNS, although IA-CL exhibits the rapid decay of the spectrum in the low-wavelength region. To quantitatively evaluate the length of the streaks, we investigate the streamwise velocity correlation function C_{xx}^{GS} defined by

$$C_{xx}^{\text{GS}}(r_x, y) = \frac{\langle \bar{u}'_x(\mathbf{x} + r_x \mathbf{e}_x) \bar{u}'_x(\mathbf{x}) \rangle}{\langle \bar{u}'_x{}^2 \rangle}, \quad (40)$$

where \mathbf{e}_x denotes the unit vector in the x direction. Figure 14 shows the streamwise velocity correlation at $y^+ = 20$ for $\text{Re}_\tau = 180$. IA reproduces a rapid decay of the correlation, while IA-LNcs42 predicts a more moderate decay. In LR, the decay of IA-LNcs42 is considerably more moderate, and the correlation does not decrease sufficiently within this domain size. This situation is similar for DSM. IA and IA-CL predict the rapid decay even in LR. IA-CL likewise predicts the rapid decay, albeit it is slightly more moderate compared with IA or f-DNS. Nevertheless, IA-CL overestimates the streamwise component of the GS velocity fluctuation, as shown in Fig. 5(a). In this sense, the SMM using the scale-similarity model for the SGS-Reynolds term is the most appropriate among the present cases in reproducing the turbulent structures including its intensity

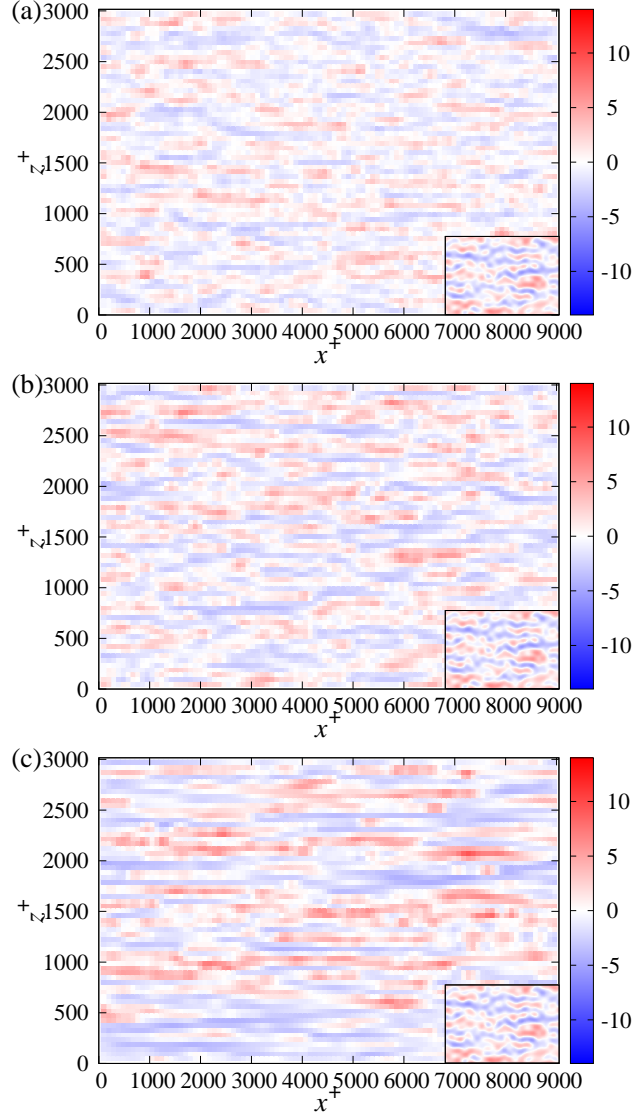


FIG. 13. Contour map of instantaneous streamwise velocity fluctuation $\bar{u}_x - \langle \bar{u}_x \rangle_{x-z\text{-plane}}$ for (a) IA180LD, (b) IA-CL180LD, (c) IA-LNcs42-180LD at $y^+ = 20$ for $Re_\tau = 180$. The bottom right inset in each figure shows the result for f-DNS with the exact domain size.

in the wall-bounded turbulent shear flow.

V. CONCLUSIONS

We investigated the physical role of various scale-similarity models in the SMM^{35,36}. The SMM proposed by Abe³⁵ adopted the scale-similarity model for the SGS-Reynolds term although, other scale-similarity models yield a better correlation with the exact SGS stress. In the present

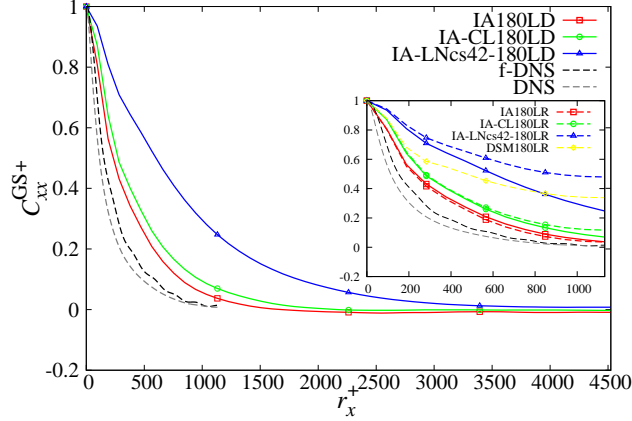


FIG. 14. Profile of streamwise velocity correlation C_{xx}^{GS} at $y^+ = 20$ for $Re_{\tau} = 180$. The right screen depicts LR cases. The result for the non-filtered DNS is plotted for reference.

study, we applied various scale-similarity models to the SMM and evaluated their performance in turbulent channel flows. As previously shown in previous studies^{16,35,38–40}, the SMM using the scale-similarity model for the SGS-Reynolds term is less sensitive to the grid resolution than the conventional eddy-viscosity models in the prediction of the mean velocity. In particular, it can predict the near-wall mean velocity profile even in coarse grid resolutions at both low- and high-Reynolds numbers. In various SMMs, the original model using the SGS-Reynolds term provides the best prediction of the Reynolds stress, whereas other models overestimate the GS streamwise velocity fluctuation. We also investigated Lumley’s invariant map⁴² to quantitatively evaluate the anisotropy of the GS and SGS turbulent stress. The result indicates that the original model predicts a similar near-wall behavior as the filtered DNS. The GS velocity fluctuations for the eddy-viscosity models result in a nearly one-component turbulence in the vicinity of the solid wall, instead of the conventional two-component state. Moreover, the eddy-viscosity model cannot predict the anisotropy of the SGS stress, which reflects the isotropic property of the eddy-viscosity model. A critical difference between various scale-similarity models is found in the spectra of the GS Reynolds stress close to the cut-off scale. The original SMM using the scale-similarity model for the SGS-Reynolds term succeeds in predicting the large intensities of the spectra close to the cut-off scale in accordance with the filtered DNS, whereas other models predict a rapid decay of the spectra in the low-wavelength region. The success of the scale-similarity model for the SGS-Reynolds term relies on the property that it is expressed by the higher-order spatial derivative, unlike other scale-similarity models.

To investigate the behavior of the models close to the cut-off scale, we analyzed the budget equation for the GS Reynolds stress spectrum^{43–45}. As a result, it was shown that the scale-similarity model for the SGS-Reynolds term plays a role in enhancing the wall-normal component of the GS velocity fluctuation close to the cut-off scale. This leads to the enhancement of the streamwise and shear components of the GS Reynolds stress in that scale through the production term. Hence, the activation of turbulence close to the cut-off scale is achieved. Owing to these properties, the streak structures observed in wall-bounded turbulent flows are successfully reproduced. Although the SMM employing the scale-similarity model for the SGS-Reynolds term does not predict the overall profiles of the budget of the GS Reynolds stress spectrum obtained from the filtered DNS, it predicts both the statistics and structures in the wall-bounded turbulent flow at the coarse grid resolution. For further development of SGS models, one should consider how to reproduce the turbulence structures including the low-wavelength region close to the cut-off scale.

ACKNOWLEDGMENTS

The authors would like to acknowledge Prof. K. Abe for valuable discussions. K. I. is grateful to Prof. F. Hamba for fruitful comments and discussions. The work of H. K. is supported in part by Keio Gijuku Academic Development Funds. We would also like to thank the referees for valuable comments for improvement of this paper.

Appendix A: Contribution of the eddy-viscosity term in SGS normal stress

Figure 15 shows the profile of the eddy-viscosity term and the EAT in the normal component of the SGS stress for IA180LR. The eddy-viscosity term is negligible compared with the EAT. IA-CL and f-DNS exhibit a similar result (not shown). The eddy-viscosity term in IA-LNcs42 is also negligible compared with the SGS kinetic energy k^{SGS} , which can be found in the Lumley invariant map in Fig. 7(b). Hence, the eddy-viscosity model cannot predict the anisotropy in turbulent channel flows.

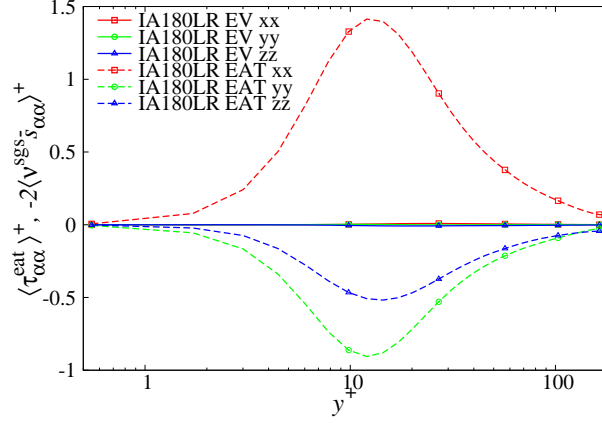


FIG. 15. Profile of the eddy-viscosity term and EAT in the normal components of SGS stress for IA180LR. Solid lines denote the eddy-viscosity term, while dashed lines denote the EAT.

Appendix B: Budget for the GS Reynolds stress

The budget equation for the GS Reynolds stress yields

$$\begin{aligned}
\frac{\partial R_{ij}^{\text{GS}}}{\partial t} + \frac{\partial}{\partial x_\ell} (U_\ell R_{ij}^{\text{GS}}) \\
= P_{ij}^{\text{GS}} - \varepsilon_{ij}^{\text{GS}} + D_{ij}^{\text{t,GS}} + \Phi_{ij}^{\text{GS}} + D_{ij}^{\text{p,GS}} + D_{ij}^{\text{v,GS}} \\
- \varepsilon_{ij}^{\text{EV}} + \xi_{ij}^{\text{EAT}} + D_{ij}^{\text{SGS}}.
\end{aligned} \tag{B1}$$

Terms on the right-hand side are similar to those in Eq. (32). Note that the inter-scale transfer term vanishes when it is summed over the wavenumbers:

$$\sum_{k_x=0}^{k_x^{\text{max}}} \check{T}_{ij}^{\text{GS}} \Delta k_x = 0. \tag{B2}$$

The trace of the pressure–strain correlation Φ_{ii}^{GS} should disappear due to incompressibility:

$$\Phi_{ii}^{\text{GS}} = 0. \tag{B3}$$

Therefore, it is sometimes referred to as the redistribution term, which plays a role of the redistribution of intensities among normal stress components. In contrast, the trace of the anisotropic redistribution term does not vanish, $\xi_{ii}^{\text{EAT}} \neq 0$, even though τ_{ij}^{eat} does not exchange energy between the GS and SGS fields, as shown in Eq. (14). This is because

$$\xi_{ii}^{\text{eat}} = 2 \langle \tau_{ij}^{\text{eat}} \bar{s}_{ij} \rangle - 2 \langle \tau_{ij}^{\text{eat}} \rangle S_{ij} = -2 \langle \tau_{ij}^{\text{eat}} \rangle S_{ij} \neq 0. \tag{B4}$$

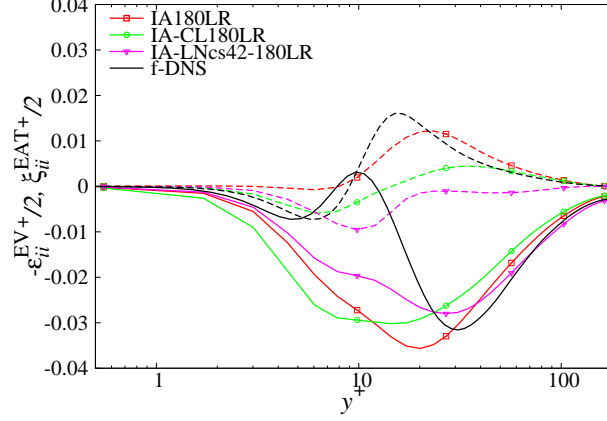


FIG. 16. Profile of trace part of the eddy-viscosity destruction $-\varepsilon_{ii}^{\text{EV}}/2$ and the anisotropic redistribution term $\xi_{ii}^{\text{EAT}}/2$ for various SMMs in LR at $\text{Re}_\tau = 180$.

The mean kinetic energy equation reads

$$\frac{\partial}{\partial t} \left(\frac{1}{2} U_i U_i \right) = -\langle \tau_{ij}^{\text{eat}} \rangle S_{ij} + \dots \quad (\text{B5})$$

Therefore, $\langle \tau_{ij}^{\text{eat}} \rangle S_{ij}$ is interpreted as the energy transfer between the mean and SGS kinetic energies, while $\xi_{ii}^{\text{EAT}}/2$ is that between the GS turbulent and SGS kinetic energies. Equation (B4) indicates that the amount energy transfer between the mean and SGS kinetic energies must be equal to that between GS and SGS turbulent kinetic energies. In other words, a change of the mean kinetic energy must be compensated as the GS turbulent kinetic energy. Thereby, $\xi_{ii}^{\text{EAT}}/2$ plays a role of the redistribution between the mean and GS turbulent kinetic energies. Hence, we named ξ_{ij}^{EAT} the anisotropic redistribution term.

Figure 16 shows the profile of the trace part of the eddy-viscosity destruction $-\varepsilon_{ii}^{\text{EV}}/2$ and the anisotropic redistribution term $\xi_{ii}^{\text{EAT}}/2$ for various SMMs in LR at $\text{Re}_\tau = 180$. For all cases, the contribution of ξ_{ii}^{EAT} is relatively small compared with $\varepsilon_{ii}^{\text{EV}}$. However, IA provides a positive ξ_{ii}^{EAT} at $y^+ = 20$ in the same manner as f-DNS, supporting the increase in the GS velocity fluctuations. The success of IA may partly lie in the property of EAT, which enhances the GS velocity fluctuations in the buffer layer $10 < y^+ < 50$.

DATA AVAILABILITY

The data that support the findings of this study are available from the corresponding author upon reasonable request.

REFERENCES

- ¹J. Smagorinsky, “General circulation experiments with the primitive equations. I. The basic experiment,” *Mon. Weather Rev.* **91**, 99 (1963).
- ²M. Germano, U. Piomelli, P. Moin, and W. H. Cabot, “A dynamic subgrid-scale eddy viscosity model,” *Phys. Fluids A* **3**, 1760 (1991).
- ³D. K. Lilly, “A proposed modification of the germano subgrid-scale closure method,” *Phys. Fluids A* **4**, 633 (1992).
- ⁴C. Meneveau, T. S. Lund, and W. H. Cabot, “A Lagrangian dynamic subgrid-scale model of turbulence,” *J. Fluid Mech.* **319**, 353 (1996).
- ⁵A. Yoshizawa and K. Horiuti, “A statistically-derived subgrid-scale kinetic energy model for the large-eddy simulation of turbulent flows,” *J. Phys. Soc. Jpn.* **54**, 2834 (1985).
- ⁶S. Ghosal, T. S. Lund, P. Moin, and K. Akselvoll, “A dynamic localization model for large-eddy simulation of turbulent flows,” *J. Fluid Mech* **286**, 229 (1995).
- ⁷F. Nicoud and F. Ducros, “Subgrid-scale stress modelling based on the square of the velocity gradient tensor,” *Flow, Turbul. Combust.* **62**, 183 (1999).
- ⁸A. W. Vreman, “An eddy-viscosity subgrid-scale model for turbulent shear flow: Algebraic theory and applications,” *Phys. Fluids* **16**, 3670 (2004).
- ⁹H. Kobayashi, “The subgrid-scale models based on coherent structures for rotating homogeneous turbulence and turbulent channel flow,” *Phys. Fluids* **17**, 045104 (2005).
- ¹⁰C. K. Aidun and J. R. Clausen, “Lattice-Boltzmann method for complex flows,” *Annu. Rev. Fluid Mech.* **42**, 439 (2010).
- ¹¹R. A. Clark, J. H. Ferziger, and W. C. Reynolds, “Evaluation of subgrid-scale models using an accurately simulated turbulent flow,” *J. Fluid Mech.* **91**, 1 (1979).
- ¹²J. Bardina, J. H. Ferziger, and W. C. Reynolds, “Improved turbulence models based on large eddy simulation of homogenous, incompressible, turbulent flows,” Report TF-19. Thermosciences Division, Dep. of Mech. Eng., Stanford University, Stanford, California (1983).
- ¹³S. Liu, C. Meneveau, and J. Katz, “On the properties of similarity subgrid-scale models as deduced from measurements in a turbulent jet,” *J. Fluid Mech.* **275**, 83 (1994).
- ¹⁴B. Tao, J. Katz, and C. Meneveau, “Statistical geometry of subgrid-scale stresses determined from holographic particle image velocimetry measurements,” *J. Fluid Mech* **457**, 35 (2002).

- ¹⁵K. Horiuti, “Roles of non-aligned eigenvectors of strain-rate and subgrid-scale stress tensors in turbulence generation,” *J. Fluid Mech* **491**, 65 (2003).
- ¹⁶H. Kobayashi, “Improvement of the SGS model by using a scale-similarity model based on the analysis of SGS force and SGS energy transfer,” *Int. J. Heat Fluid Flow* **72**, 329 (2018).
- ¹⁷K. Horiuti, “The role of the Bardina model in large eddy simulation of turbulent channel flow,” *Phys. Fluids A* **1**, 426 (1989).
- ¹⁸K. Horiuti, “Backward scatter of subgrid-scale energy in wall-bounded and free shear turbulence,” *J. Phys. Soc. Jpn.* **66**, 91 (1997).
- ¹⁹U. Piomelli, P. Moin, and J. H. Ferziger, “Model consistency in large eddy simulation of turbulent channel flows,” *Phys. Fluids* **31**, 1884 (1988).
- ²⁰Y. Zang, R. L. Street, and J. R. Koseff, “A dynamic mixed subgrid-scale model and its application to turbulent recirculating flows,” *Phys. Fluids A* **5**, 3186 (1993).
- ²¹B. Vreman, B. Geurts, and H. Kuerten, “On the formulation of the dynamic mixed subgrid-scale model,” *Phys. Fluids* **6**, 4057 (1994).
- ²²M. V. Salvetti and S. Banerjee, “*A priori* tests of a new dynamic subgrid-scale model for finite-difference large-eddy simulations,” *Phys. Fluids* **7**, 2831 (1995).
- ²³K. Horiuti, “A new dynamic two-parameter mixed model for large-eddy simulation,” *Phys. Fluids* **9**, 3443 (1997).
- ²⁴R. Anderson and C. Meneveau, “Effects of the similarity model in finite-difference LES of isotropic turbulence using a Lagrangian dynamic mixed model,” *Flow, Turbul. Combust.* **62**, 201 (1999).
- ²⁵F. Sarghini, U. Piomelli, and E. Balaras, “Scale-similar models for large-eddy simulations,” *Phys. Fluids* **11**, 1596 (1999).
- ²⁶Y. Morinishi and O. V. Vasilyev, “A recommended modification to the dynamic two-parameter mixed subgrid scale model for large eddy simulation of wall bounded turbulent flow,” *Phys. Fluids* **13**, 3400 (2001).
- ²⁷B. W. Anderson and J. A. Domaradzki, “A subgrid-scale model for large-eddy simulation based on the physics of interscale energy transfer in turbulence,” *Phys. Fluids* **24**, 065104 (2012).
- ²⁸S. B. Pope, “A more general effective-viscosity hypothesis,” *J. Fluid Mech.* **72**, 331 (1975).
- ²⁹A. Yoshizawa, “Statistical analysis of the derivation of the Reynolds stress from its eddy-viscosity representation,” *Phys. Fluids* **27**, 1377 (1984).

- ³⁰T. B. Gatski and C. G. Speziale, “On explicit algebraic stress models for complex turbulent flows,” *J. Fluid Mech.* **254**, 59 (1993).
- ³¹S. Wallin and A. V. Johansson, “An explicit algebraic Reynolds stress model for incompressible and compressible turbulent flows,” *J. Fluid Mech.* **403**, 89 (2000).
- ³²L. Marstorp, G. Brethouwer, O. Grundestam, and A. V. Johansson, “Explicit algebraic subgrid stress models with application to rotating channel flow,” *J. Fluid Mech.* **639**, 403 (2009).
- ³³M. Montecchia, G. Brethouwer, A. V. Johansson, and S. Wallin, “Taking large-eddy simulation of wall-bounded flows to higher Reynolds numbers by use of anisotropy-resolving subgrid models,” *Phys. Rev. Fluids* **2**, 034601 (2017).
- ³⁴M. Montecchia, G. Brethouwer, S. Wallin, A. V. Johansson, and T. Knacke, “Improving LES with OpenFOAM by minimising numerical dissipation and use of explicit algebraic SGS stress model,” *J. Turbulence* **20**, 697 (2019).
- ³⁵K. Abe, “An improved anisotropy-resolving subgrid-scale model with the aid of a scale-similarity modeling concept,” *Int. J. Heat Fluid Flow* **39**, 42 (2013).
- ³⁶M. Inagaki and K. Abe, “An improved anisotropy-resolving subgrid-scale model for flows in laminar–turbulent transition region,” *Int. J. Heat Fluid Flow* **64**, 137 (2017).
- ³⁷M. Klein, S. Ketterl, L. Engelmann, A. Kempf, and H. Kobayashi, “Regularized, parameter free scale similarity type models for large eddy simulation,” *Int. J. Heat Fluid Flow* **81**, 108496 (2020).
- ³⁸T. Ohtsuka and K. Abe, “On the role of an anisotropy-resolving extra term for a subgrid-scale model in near-wall turbulence,” *J. Comput. Sci. Technol.* **7**, 410 (2013).
- ³⁹K. Abe, “An investigation of SGS-stress anisotropy modeling in complex turbulent flow fields,” *Flow, Turbul. Combust.* **92**, 503 (2014).
- ⁴⁰K. Abe, “Notable effect of the subgrid-scale stress anisotropy on mean-velocity prediction through budget of the grid-scale Reynolds-shear stress,” *Phys. Fluids* **31**, 105103 (2019).
- ⁴¹K. Horiuti, “A proper velocity scale for modeling subgrid-scale eddy viscosities in large eddy simulation,” *Phys. Fluids A* **5**, 146 (1993).
- ⁴²K. Hanjalić and B. Launder, *Modelling Turbulence in Engineering and the Environment: Second-Moment Routes to Closure* (Cambridge University Press, Cambridge, 2011).
- ⁴³Y. Mizuno, “Spectra of energy transport in turbulent channel flows for moderate Reynolds numbers,” *J. Fluid Mech.* **805**, 171 (2016).

- ⁴⁴T. Kawata and P. H. Alfredsson, “Inverse interscale transport of the Reynolds shear stress in plane Couette turbulence,” *Phys. Rev. Lett.* **120**, 244501 (2018).
- ⁴⁵M. Lee and R. D. Moser, “Spectral analysis of the budget equation in turbulent channel flows at high Reynolds number,” *J. Fluid Mech.* **860**, 886 (2019).
- ⁴⁶S. B. Pope, *Turbulent Flows* (Cambridge University Press, Cambridge, 2000).
- ⁴⁷C. G. Speziale, “Galilean invariance of subgrid-scale stress models in the large-eddy simulation of turbulence,” *J. Fluid Mech.* **156**, 55 (1985).
- ⁴⁸M. Germano, “A proposal for a redefinition of the turbulent stresses in the filtered Navier–Stokes equations,” *Phys. Fluids* **29**, 2323 (1986).
- ⁴⁹M. Inagaki, “A new wall-damping function for large eddy simulation employing Kolmogorov velocity scale,” *Int. J. Heat Fluid Flow* **32**, 26 (2011).
- ⁵⁰Y. Morinishi, T. S. Lund, O. V. Vasilyev, and P. Moin, “Fully conservative higher order finite difference schemes for incompressible flow,” *J. Comput. Phys.* **143**, 90 (1998).
- ⁵¹T. Kajishima and K. Taira, *Computational Fluid Dynamics* (Springer, New York, 2017).
- ⁵²M. Lee and R. D. Moser, “Direct numerical simulation of turbulent channel flow up to $re_\tau \approx 5200$,” *J. Fluid Mech.* **774**, 395 (2015).
- ⁵³S. J. Kline, W. C. Reynolds, F. A. Schraub, and P. W. Runstadler, “The structure of turbulent boundary layers,” *J. Fluid Mech.* **30**, 741 (1967).
- ⁵⁴U. Schumann, “Realizability of Reynolds-stress turbulence models,” *Phys. Fluids* **20**, 721 (1977).
- ⁵⁵B. Vreman, B. Geurts, and H. Kuerten, “Realizability conditions for the turbulent stress tensor in large-eddy simulation,” *J. Fluid Mech.* **278**, 351 (1994).
- ⁵⁶J. M. Hamilton, J. Kim, and F. Waleffe, “Regeneration mechanisms of near-wall turbulence structures,” *J. Fluid Mech.* **287**, 317 (1995).
- ⁵⁷F. Waleffe, “On a self-sustaining process in shear flows,” *Phys. Fluids* **9**, 883 (1997).
- ⁵⁸P. Moin and J. Kim, “Numerical investigation of turbulent channel flow,” *J. Fluid Mech.* **118**, 341 (1982).